AD-A145 674 OPTICAL WAVEGUIDE SPATIAL FILTERS(U) BATTELLE COLUMBUS LABS OH C M VERBER ET AL. 31 MAY 84 AFOSR-TR-84-0811 F49620-79-C-0044 1/1

UNCLASSIFIED F/G 20/6 NL

END

FILMED

DTIC

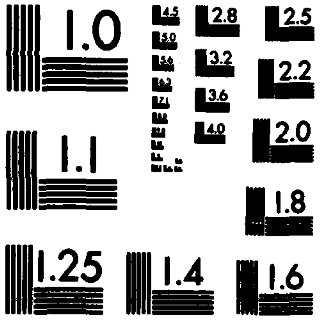

MICROCOPY RESOLUTION TEST CHART
NATIONAL BUREAU OF STANDARDS-1963-A

AFOSR-TR- 84 0811

10

FINAL REPORT

on

OPTICAL WAVEGUIDE SPATIAL FILTERS

to

AIR FORCE OFFICE OF SCIENTIFIC RESEARCH

by

C. M. Verber, R. P. Kenan
J. R. Busch and M. Parmenter

May 31, 1984

DTIC
ELECTE
S SEP 20 1984 D
B

BATTELLE-COLUMBUS LABORATORIES
505 King Avenue
Columbus, Ohio 43201

DISTRIBUTION STATEMENT A
Approved for public release;
Distribution Unlimited

84 09 17 025

FINAL REPORT

on

OPTICAL WAVEGUIDE SPATIAL FILTERS

to

AIR FORCE OFFICE OF SCIENTIFIC RESEARCH

by

C. M. Verber, R. P. Kenan
J. R. Busch and M. Parmenter

May 31, 1984

BATTELLE-COLUMBUS LABORATORIES
505 King Avenue
Columbus, Ohio 43201

UNCLASSIFIED

SECURITY CLASSIFICATION OF THIS PAGE *(When Data Entered)*

REPORT DOCUMENTATION PAGE

READ INSTRUCTIONS
BEFORE COMPLETING FORM

1. REPORT NUMBER AFOSR-TR- 84 - 0811	2. GOVT ACCESSION NO.	3. RECIPIENT'S CATALOG NUMBER
4. TITLE *(and Subtitle)* OPTICAL WAVEGUIDE SPATIAL FILTERS		5. TYPE OF REPORT & PERIOD COVERED Final Report 6. PERFORMING ORG. REPORT NUMBER
7. AUTHOR(s) C. M. Verber, R. P. Kenan, J. R. Busch and M. Parmenter		8. CONTRACT OR GRANT NUMBER(s) F49620-79-C-0044
9. PERFORMING ORGANIZATION NAME AND ADDRESS Battelle Columbus Laboratories 505 King Avenue Columbus, Ohio 43201		10. PROGRAM ELEMENT, PROJECT, TASK AREA & WORK UNIT NUMBERS 61102F, 2305/B1
11. CONTROLLING OFFICE NAME AND ADDRESS Air Force Office of Scientific Research Building 410 Bolling AFB, Washington, D.C. 20332		12. REPORT DATE ~~March 1984~~ May 84 13. NUMBER OF PAGES 57
14. MONITORING AGENCY NAME & ADDRESS *(if different from Controlling Office)*		15. SECURITY CLASS. *(of this report)* UNCLASSIFIED 15a. DECLASSIFICATION/DOWNGRADING SCHEDULE

16. DISTRIBUTION STATEMENT *(of this Report)*

Approved for public release;
distribution unlimited.

17. DISTRIBUTION STATEMENT *(of the abstract entered in Block 20, if different from Report)*

18. SUPPLEMENTARY NOTES

19. KEY WORDS *(Continue on reverse side if necessary and identify by block number)*

$LiNbO_3$	Optical Gratings
Integrated Optics	Electrooptic Effect
Waveguides	Matrix Multiplication
Optical Processing	D/A Conversion
Optical Computing	

20. ABSTRACT *(Continue on reverse side if necessary and identify by block number)*

This report deals with the continued development of analog computational devices using planar Ti-indiffused $LiNbO_3$ waveguide technology. A previously developed integrated optical spatial light modulator is used to implement a electrical-digital to optical-analog converter. Designs for matrix-vector and matrix-matrix multipliers are developed and detailed characterization of an electrooptic "herringbone" electrode structure which is used in these devices is presented.

DD FORM 1 JAN 73 1473

Unclassified

SECURITY CLASSIFICATION OF THIS PAGE *(When Data Entered)*

TABLE OF CONTENTS

LIST OF FIGURES

LIST OF FIGURES
(Continued)

LIST OF FIGURES
(Continued)

LIST OF TABLES

I. INTRODUCTION

This program was initiated on March 1, 1979, with the goal of developing an optical waveguide spatial filter which could be of use in a variety of integrated optical signal-processing devices. This initial effort resulted in the design, fabrication and testing of an integrated optical spatial light modulator (IOSLM) which consists of a multiply addressable electrooptic grating array capable of hundred-megahertz operation.

The IOSLM was then used as one of the key elements in an integrated optical digital correlator which operated on 32-bit words at a data rate of 32 MBit/sec. Variations of the electrooptic grating transducer were also used to produce devices which performed subtraction and vector subtraction. In addition, the IOSLM formed the basis for a variety of concepts for devices such as a graphics character generator and a very high-speed parallel-to-serial converter which could be used for time-domain multiplexing. These results were dealt with in detail in an Annual Report dated June 30, 1982 and, with the exception of a brief section on electrooptic gratings which is required to make this report a self-contained document, will not be repeated here.

Since the completion of the correlator work, this program has been devoted to the exploration of integrated optical techniques for matrix multiplication. We have concentrated upon planar- as opposed to channel-waveguide techniques, and a variety of approaches based upon the use of electrooptic grating arrays have been conceived. Designs for both fully-parallel devices and multipliers based upon variations of the systolic-array architecture are presented in Section III of this report.

In Section IV we discuss an IOSLM-based D/A converter which was developed specifically to facilitate the interfacing of one of the multipliers with a high-speed, parallel digital data stream. A laboratory version of the device was successfully tested.

The major experimental activity in this phase of the program was the design and testing of the "herringbone" electrode structure which is the basis for the multiplication devices. The design and fabrication of this device and a series of static tests of its properties are described in Sections V and VI. The tests run on this first version of the herringbone electrode revealed some cross-talk problems and also suggested that second-order diffraction may be a difficulty. Interpretation of these results suggests ways in which these problems may be solved. There is, therefore, every reason to believe that this work will lead to future generations of high-performance matrix multipliers.

II. ELECTROOPTIC GRATINGS AND THE IOSLM

THE ELECTROOPTIC GRATING

The matrix multiplication devices which are discussed in this report all employ a planar electrooptic waveguide, such as Ti-indiffused $LiNbO_3$(1), upon which are fabricated arrays of electrooptic grating modulators. A linear array of such modulators is referred to as an "integrated optical spatial light modulator" or IOSLM.

The basic geometry of the surface electrodes which are used to induce the electrooptic gratings is shown in Figure 1. The electrodes are defined on the waveguide surface by standard photolithographic techniques. A sputtered glass buffer layer is usually employed(2) to isolate the guided wave from perturbation by the metallization pattern. It is conventional to make the electrode line-width equal the spacing between adjacent fingers, so the required photolithographic resolution is $\Lambda/4$.

As indicated in Figure 2, the application of a voltage across the electrodes results in a periodic electric field which, via the electrooptic effect, gives rise to a periodic modulation of the index of refraction of the waveguide material and thus to the mode index of the guided wave. The guided wave sees this periodic perturbation as a thick phase grating and will be diffracted as indicated in Figure 1 when incident upon the grating at the Bragg angle, defined by

$$\sin\theta_B = \frac{\lambda}{2\Lambda} \qquad (1)$$

where λ is the optical wavelength in the medium.

The diffraction efficiency(3) is

$$\eta = \sin^2 \frac{\pi \Delta n d}{\lambda_o \cos\theta_B} \qquad (2)$$

where Δn is the amplitude of the periodic index modulation. The magnitude of Δn is determined by the product of the applied field strength E and the appropriate electrooptic coefficient r_{ij} according to(4)

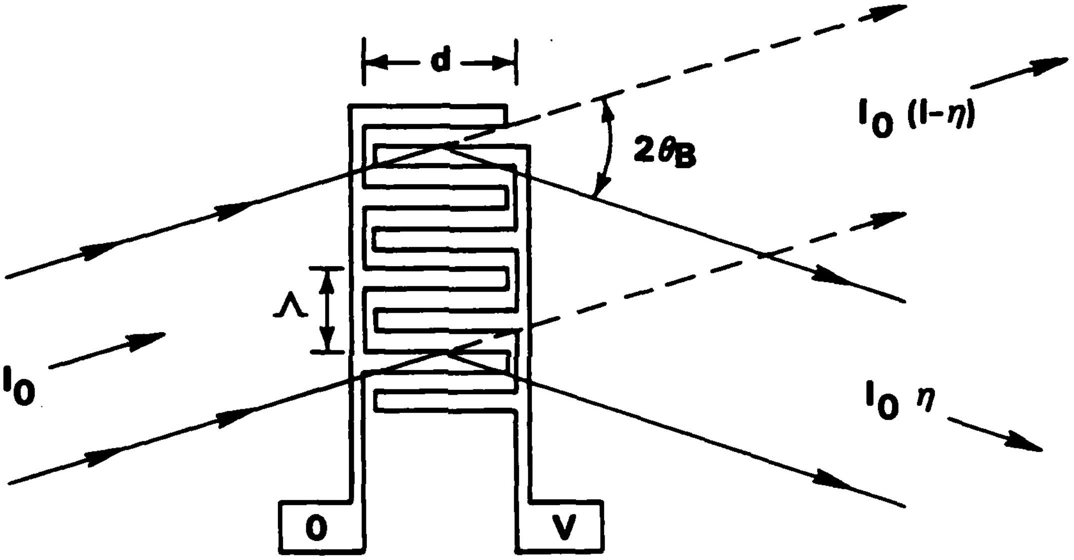

Figure 1. Electrode geometry for an electrooptic grating transducer. The diffraction efficiency η is a function of the applied voltage.

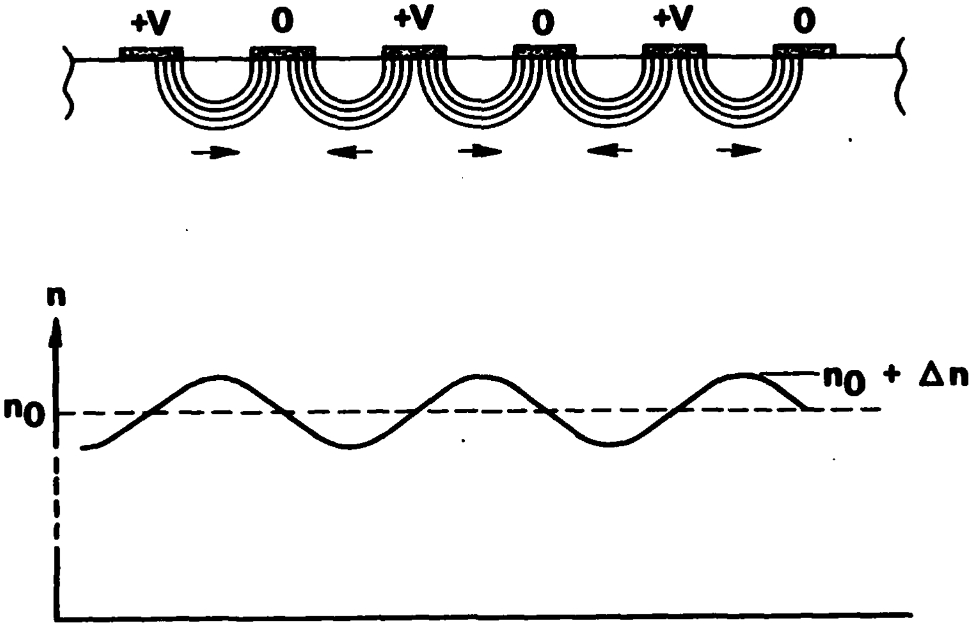

Figure 2. Top) cross-section of the EO grating transducer showing the electric field pattern and bottom) the resultant index modulation due to the electrooptic effect.

$$\Delta n = \frac{1}{2} n^3 r_{ij} E \tag{3}$$

where n is the average index of refraction. Inclusion of geometric effects(5) results in an index modulation

$$\Delta n = \frac{1}{2} n^3 r_{ij} \frac{2}{\pi} \left(\frac{V}{\Lambda/4}\right) \tag{4}$$

or a diffraction efficiency of

$$\eta(V) = \sin^2 \left(\frac{4n^3 r_{ij}\, d}{\lambda_o \cos\theta_B} V\right) \tag{5}$$

Ignoring buffer layer effects, Eq. (5) indicates that for $\Lambda = 8$ µm, a He-Ne laser and d = 2 mm, we get 100% diffraction efficiency for V = 3.1 volts. Since high diffraction efficiencies are readily achieved and the electrode capacitances are quite low, it is evident that the electrooptic Bragg effect can be utilized to make a high performance modulator. This device was originally suggested by Hammer and Phillips (6) and has more recently been employed by Holman(7) to make a high performance planar modulator with a 69% optical throughput.

THE INTEGRATED OPTICAL SPATIAL LIGHT MODULATOR

The basic grating structure can be extended as shown in Figure 3 by introducing electrodes which allow segments of the grating to be individually addressed. In this manner, one can impose a transverse amplitude modulation upon the diffracted beam. The undiffracted beam will of course have a complementary modulation. The grating structure is now operating as an electrically addressable integrated optical spatial light modulator (IOSLM) and can in principle be used to modulate an arbitrarily wide guided wave. The modulator can be used in an analog or a binary mode, although there will obviously be a finite number of addressable segments. The largest such IOSLM we have fabricated thus far(8) is composed of 32 200-µm-wide segments and spans a 6.4 mm-wide guided wave.

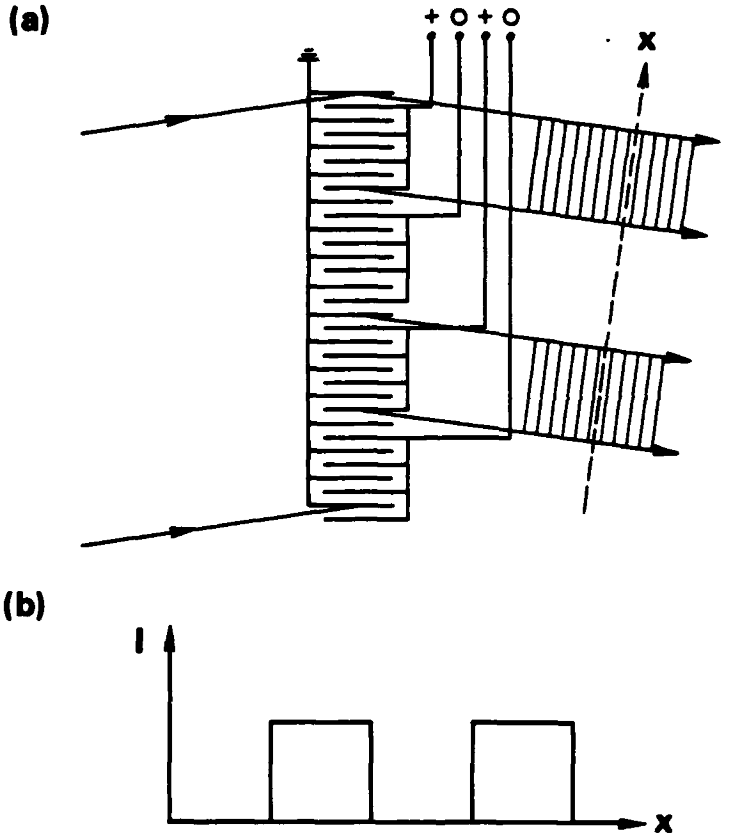

Figure 3. a) Schematic of an integrated optical spatial light modulator with alternate segments energized. The idealized optical intensity distribution is shown in b).

Optical Multiplication

There are currently two methods of performing the operation of multiplication using optical carriers. The first uses an amplitude-modulated source followed by an intensity modulator. The other method uses a constant-amplitude source and two successive modulators. Although optical elements with linear gain may be available in the future, the use of attenuators currently limits us to products of numbers each of which is between zero and one. An electro-optic grating structure which incorporates two modulators and can therefore be used for multiplication as shown in Figure 4.

The electrode structure which, for obvious reasons, is referred to as a "herringbone" electrode, consists of two grating modulators with a common spine. The modulators are tilted with respect to each other so that light diffracted by the first, enters the second modulator at its Bragg angle. Light exiting the second modulator has a intensity which is proportional to the product of the diffraction efficiencies of the two halves of the herringbone. Of course, the herringbone would function just as well if the two modulators were spatially separated.

The multiplication concept can be extended by forming each half of the herringbone out of an N-segment IOSLM (Figure 5). If the segments of each side of the extended herringbone structure are properly excited by voltages which correspond to the components of two vectors as shown in the figure, then the sum of all of the components of the doubly-diffracted light is proportional to the scalar product of the two vectors.

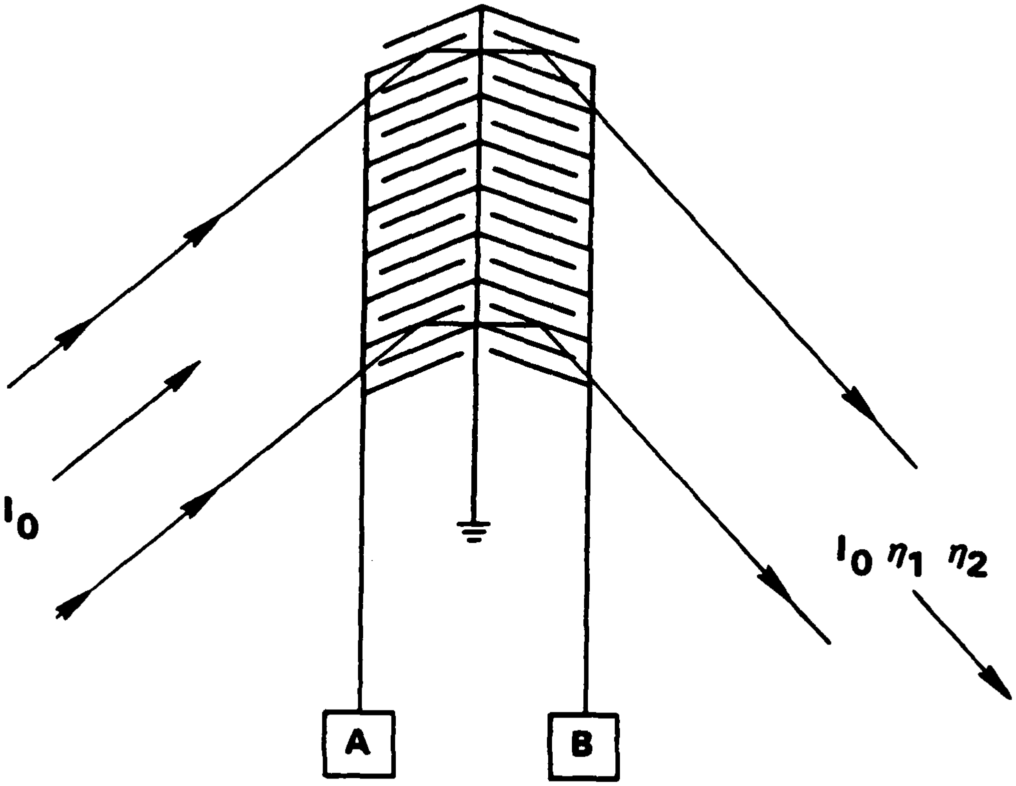

Figure 4. A symmetric herringbone electrode structure for performing multiplication. η_1 and η_2 are proportional to the voltages A and B, respectively.

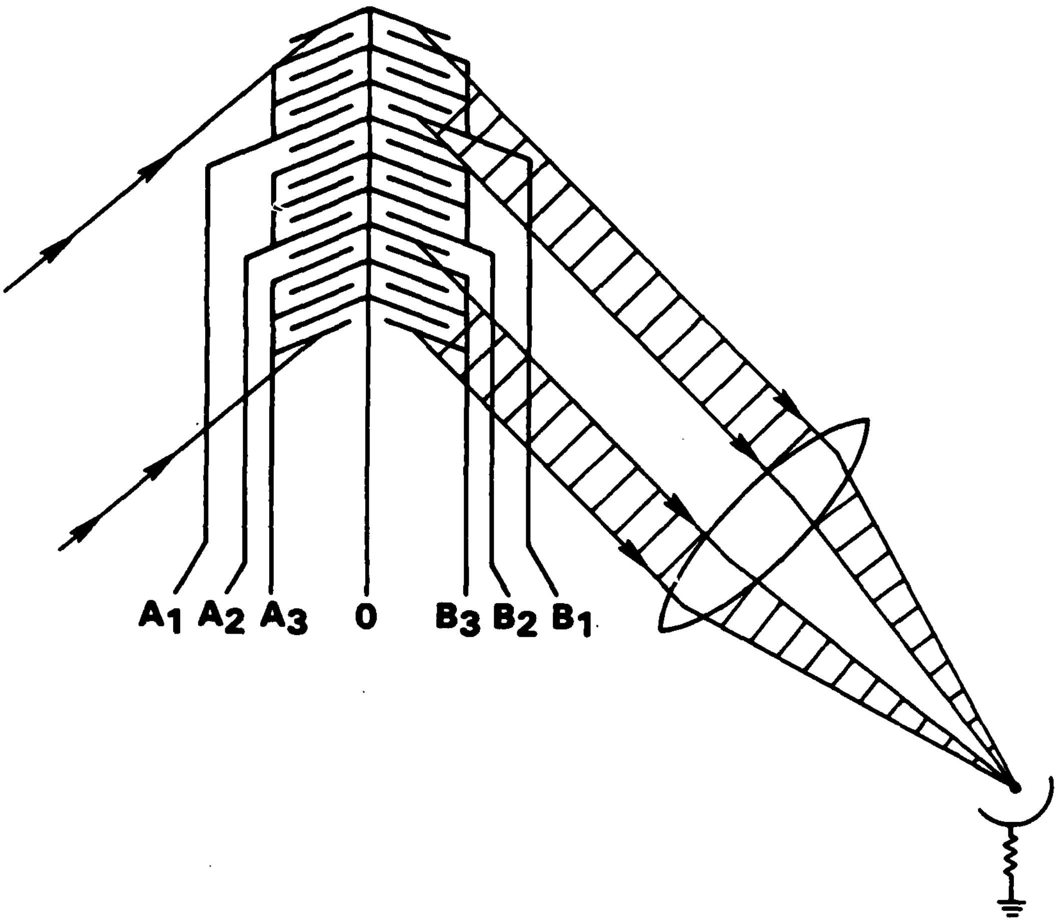

Figure 5. A segmented herringbone electrode in conjunction with a lens on a planar electrooptic waveguide can be used to produce the vector product $\vec{A} \cdot \vec{B}$.

Linearity

Most analog optical modulators are intrinsically nonlinear since their response to an applied voltage V is to reduce an initial optical intensity I_0 to an intensity

$$I = I_0 \sin^2 kV. \qquad (6)$$

The problem of deriving a linear output from these intrinsically nonlinear devices can be handled in several ways, none of which is without its limitations. A linear output can be obtained at the expense of dynamic range and the introduction of a zero offset by operating the modulator in such a way that the argument of the sine function is limited to a small range around $\pi/4$.

A second approach is to use an analog circuit such as that shown in Figure 6, to generate a voltage

$$V(x) = (\sin^{-1} \sqrt{x})/k \qquad (7)$$

which when applied to the modulator will result in an output $I(x) = I_0 x$. The tradeoff here is a loss of speed due to the response time of the analog electronics.

A third approach is to use the analog modulator as an A/D converter. Such a converter and its use in integrated optical multipliers are discussed in Section IV.

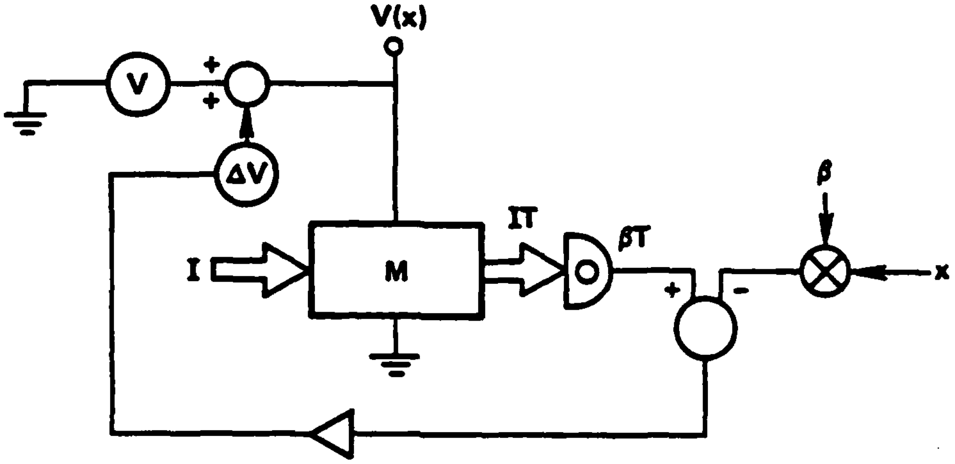

Figure 6. Circuit for generating $V(x) = (\sin^{-1}\sqrt{x})/k$. M is an electrooptic grating modulator for which $T = \sin^2 kV(x)$.

III. ARCHITECTURES FOR INTEGRATED OPTICAL MATRIX MULTIPLIERS

MATRIX-VECTOR MULTIPLICATION

A Parallel Approach

Much of the current work on numerical optical processors stems from the concept of the fully-parallel matrix-vector multiplier which was published by Goodman and his coworkers at Stanford in 1978(9). As shown in Figure 7, vector components are introduced as LED intensities and the matrix elements as the transmissivity of windows in a mask. Appropriate anamorphic optics are used to properly distribute the light over the matrix mask and to direct it onto the appropriate detectors. This architecture has the advantage of very high processing speed as the result of its parallelism. Its three-dimensional format immediately serves to point out one of the limitations of integrated optics in that some manipulation is required to duplicate the operation of the Stanford device in a planar geometry.

A design for an integrated optical circuit (IOC) for performing fully parallel matrix-vector multiplication is shown in Figure 8(10). Voltages representing the vector components are applied to the segments of an IOSLM. A guided plane wave passing under the IOSLM is modulated by the resulting electrooptic grating and carries this information under a set of grating beam splitters which distribute the light so that it passes under a second set of electrooptic gratings. This second set of gratings is activated by voltages which represent the matrix elements. The sets of products which result from the action of the two sets of modulators on the light beams are summed by being combined on the detectors by the lenses. This scheme is superior to the Stanford device in that the matrix values can be varied as easily as the vector components. On the other hand, the planar geometry forces the matrix-element modulators to be arranged in a line which is N^2-units long. This is much less convenient than the N x N array allowed by the 3-D geometry and will ultimately limit the size of the device.

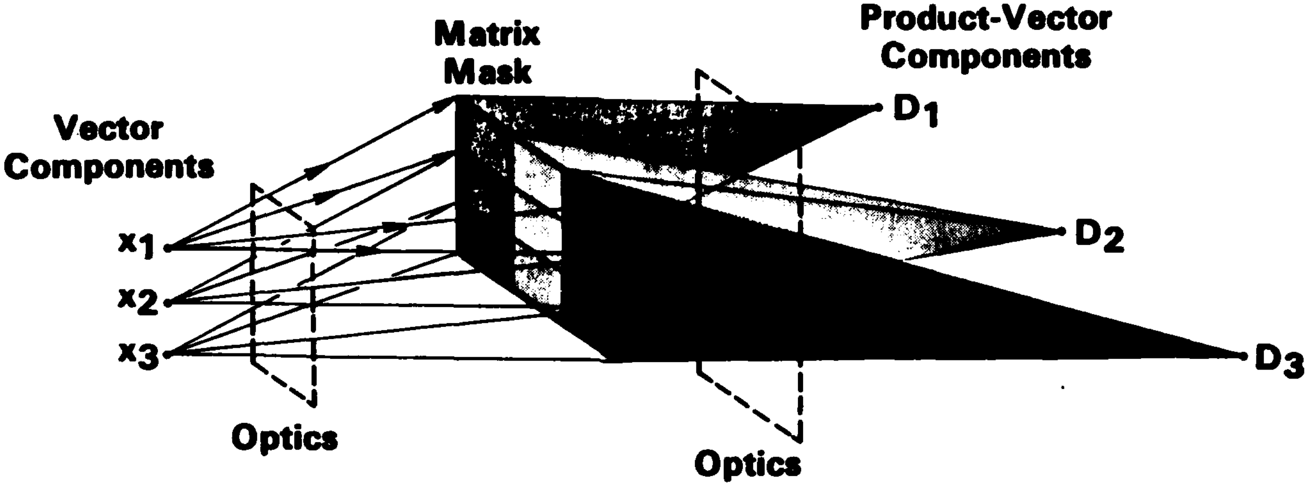

Figure 7. Schematic of the Stanford fully-parallel matrix-vector multiplier. The x_1 are introduced as LED intensities.

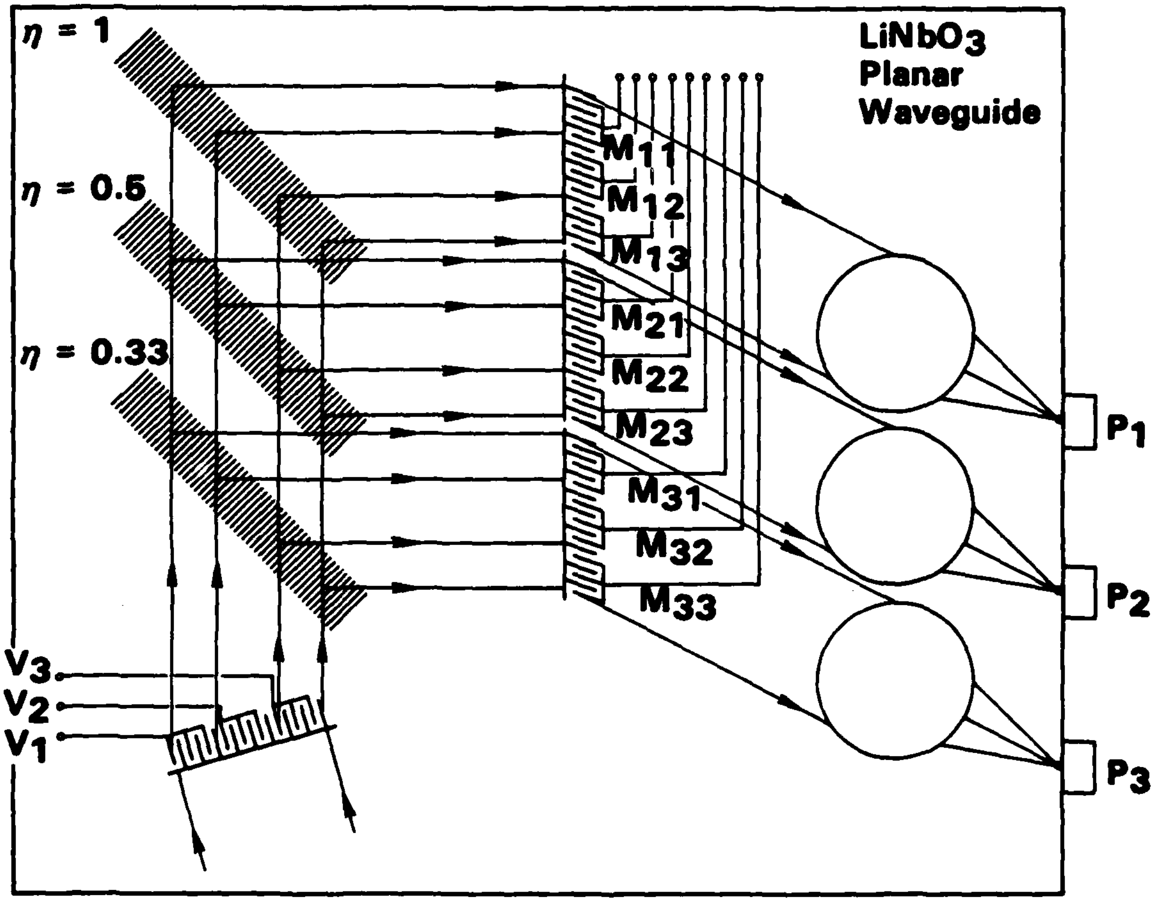

Figure 8. An IOC for fully-parallel vector matrix multiplication.

Approaches Based on the Systolic Array Processor

The systolic array architecture was developed by Kung(11) and others as a method for improving the efficiency of VLSI processors. The basic concept is that of a series of identical processors through which data are clocked in such a way that the desired results accumulate under the conditions that only nearest-neighbor processors communicate and that the data are entered into the array only once.

The first optical adaptation of the systolic algorithm was suggested by Caulfield et al(12) who proposed the Bragg cell processor shown in Figure 9. Here, the values corresponding to the matrix elements are introduced as LED intensities, the vector components as acoustic intensities, and the products are summed by a CCD detector array which is clocked in synchronism with the acoustic wave so that the products end up in the appropriate bins.

An improvement in this architecture was subsequently suggested by Tamura(13). The advantages of this new "engagement architecture" are that the spaces between the data required by the systolic arrangement are eliminated, and that the proper products all arrive at the same spot so that the tracking CCD array can be replaced by a stationary detector array. The systolic and the engagement architectures for matrix-vector multiplication are compared in Figure 10. Note that in both cases it is necessary to skew the matrix to obtain proper registration of the matrix and vector components in the engagement region. The advantage of the systolic and the engagement architectures, from the point of view of integrated optics, is that they both are naturally implemented in a planar geometry. This occurs since the clocking of the data, in effect, replaces a spatial dimension with time.

Although it would have been possible to directly implement Figure 9, or its engagement version in an integrated-optical format, we chose to use an electrooptic approach rather than the acoustooptic approach in designing an IOC for matrix-vector multiplication. This was done for several reasons.

- Our experience with electrooptic gratings indicated that near-100% diffraction efficiency could be obtained with low working voltages.

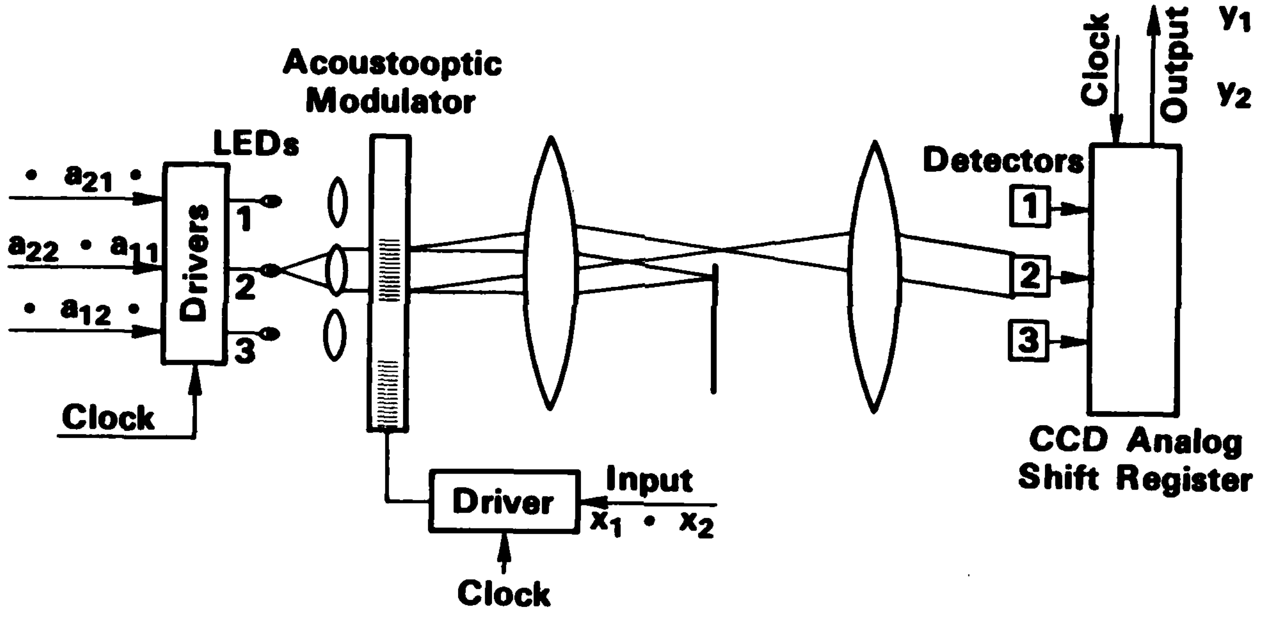

Figure 9. Suggestion(12) for an optical systolic processor for matrix-vector multiplication.

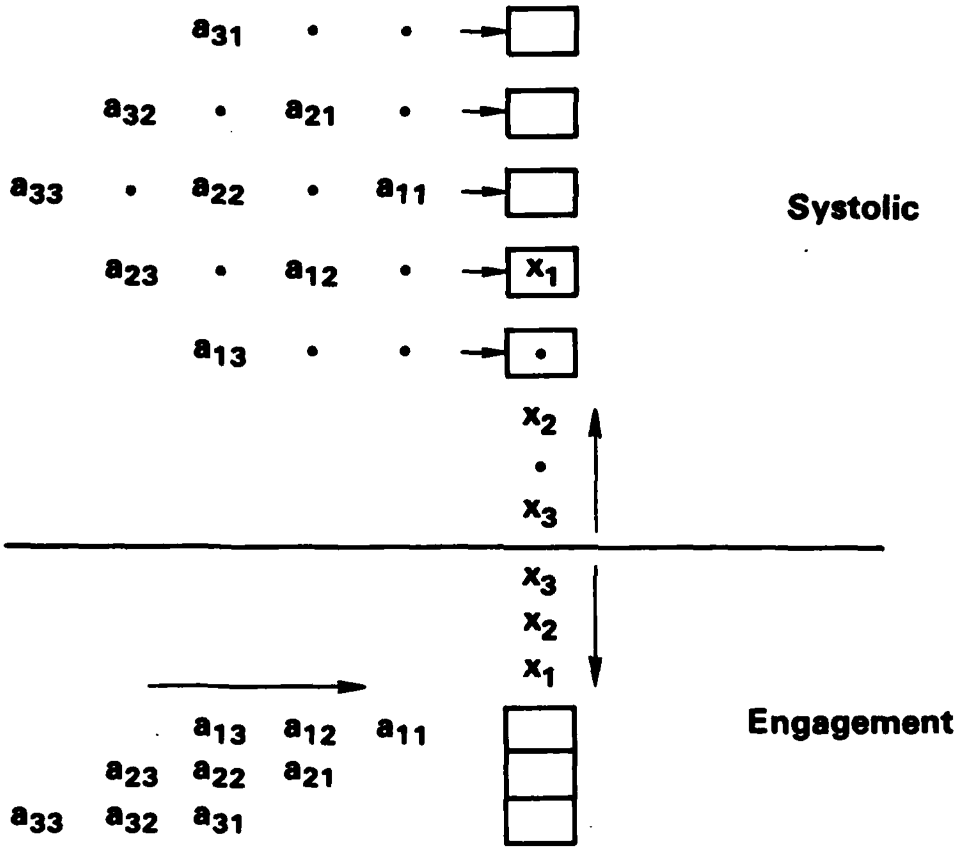

Figure 10. Comparison of systolic and engagement architecture for matrix-vector multiplication.

- Our experience with the correlator taught us that precise synchronization between the SAW and the data rate has to be maintained. This means that device dimensions are dictated by the acoustic velocity which may change with device temperature.
- We felt that shift registers would require less power than the r.f. oscillators required to drive the SAW.

The result of these considerations led to the design of the integrated optical engagement processor for matrix-vector multiplication shown in Figure 11. It consists of a planar $LiNbO_3$ waveguide with a butt-coupled laser diode whose collimated output illuminates a segmented herringbone electrode. The electrodes constitute the engagement region which is imaged on a butt-coupled detector array.

Also shown in Figure 11 is an indication of the electronics which are required to run the engagement processor. The assumption has been made that the matrix elements are stored in a digital memory and are updated slowly, if at all. The data, in the form of vector components, arrive serially. Note that, contrast to the parallel approach, it is necessary to manipulate the matrix components at the data rate for the engagement device to function. This leads to additional electronic complexity. This is shown more explicitly in Figure 12 which is a more detailed diagram of the electronic circuitry which is required to carry out complete tests of the engagement multiplier.

The principal trade-off between the parallel and the engagement architectures is that the former requires much simpler electronics and the latter is much simpler optically. In addition to having no beam splitters, the engagement device has an N- rather than N^2-element IOSLM. Features of the two approaches to matrix-vector multiplication are compared in Table 1.

MATRIX-MATRIX MULTIPLICATION

Because of the dimensional limitations of integrated optics it does not seem possible to devise a reasonable fully-parallel approach to matrix-matrix multiplication. We have, however, devised several methods which are

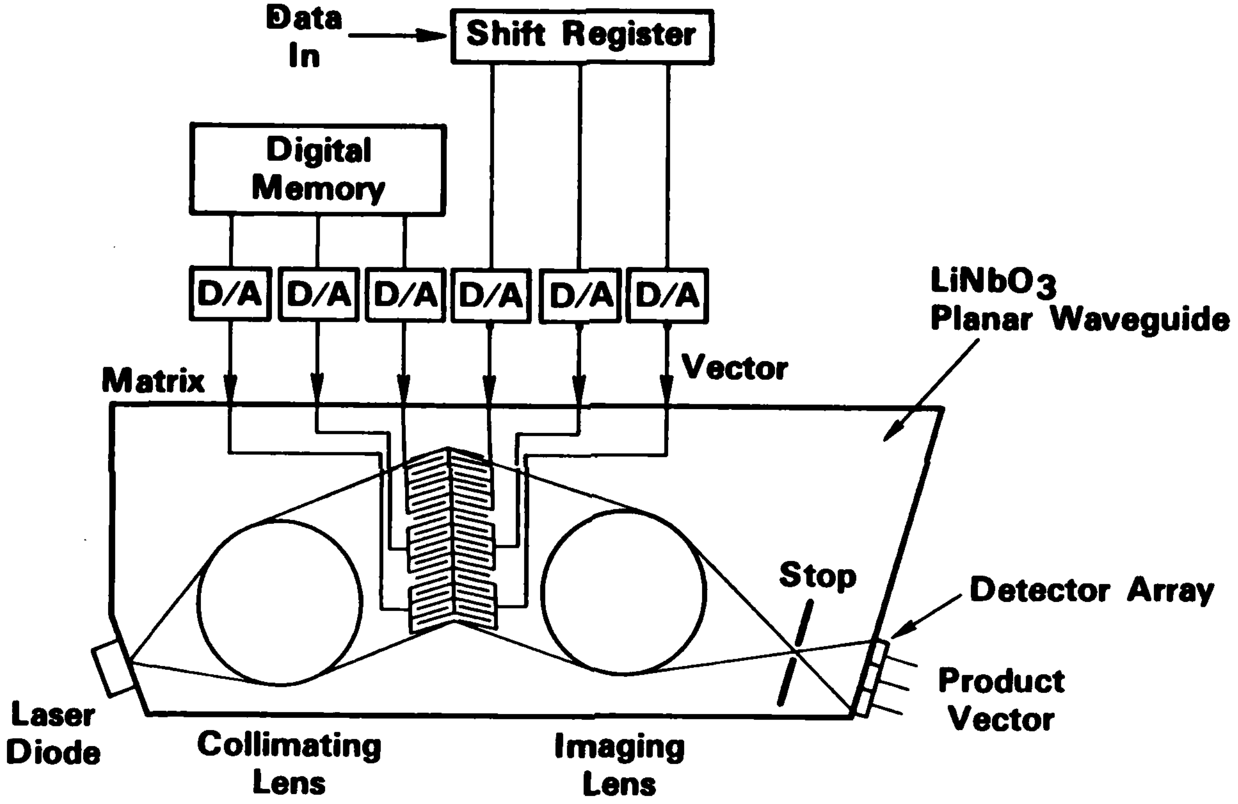

Figure 11. Schematic of an IO engagement matrix-vector multiplier. The beam stop keeps all but the twice-diffracted light from reaching the detector array.

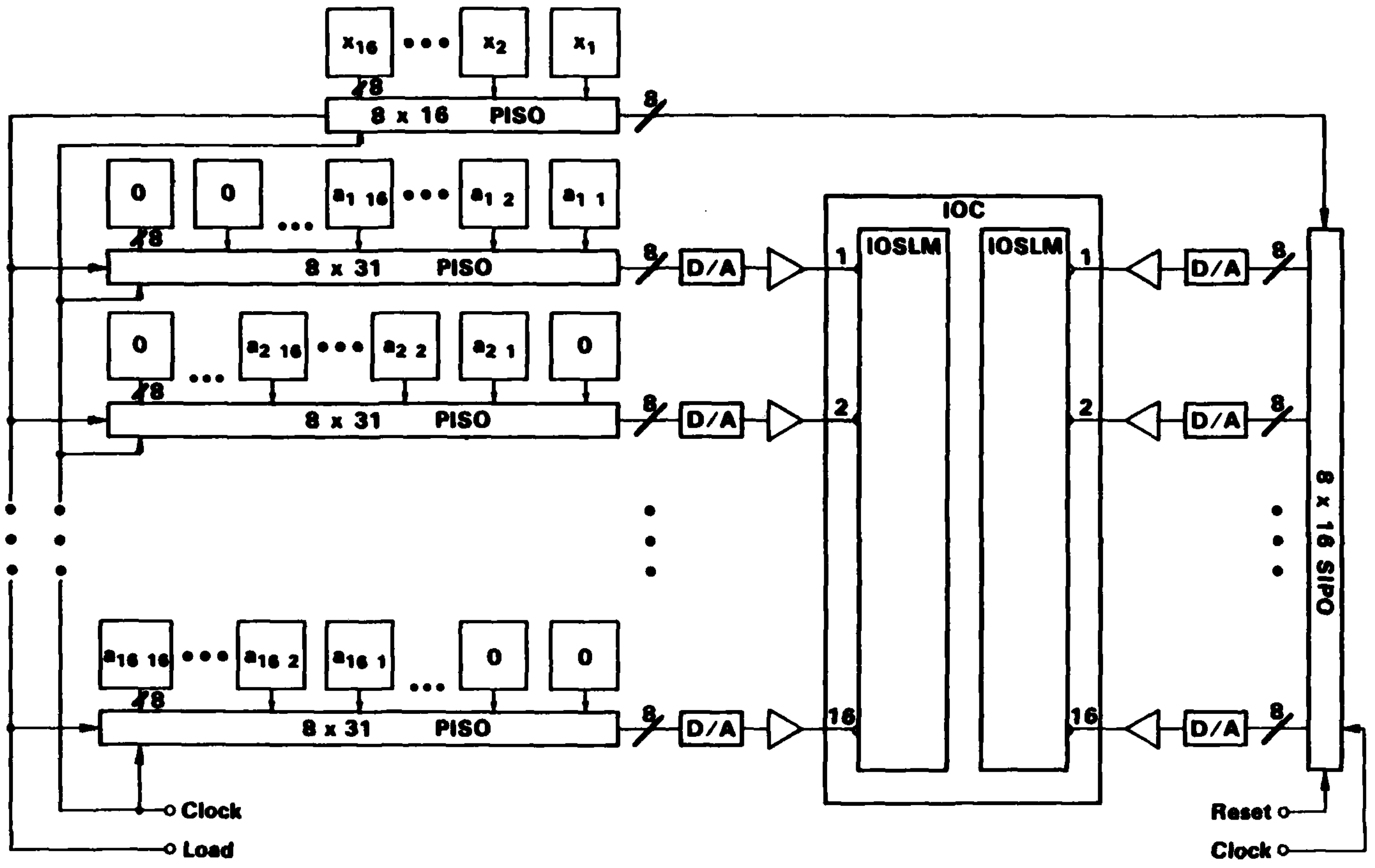

Figure 12. Expanded schematic of digital drive circuit for the engagement matrix-vector multiplier.

TABLE 1. COMPARISON OF DIRECT AND ENGAGEMENT ARCHITECTURES

	Engagement	Direct
Data Flow	Stepped	Continuous
Electronic Interface	Parallel set of sequential inputs	Fully parallel
Natural Device Geometry	Planar	3-D
Speed	Limited by electronic clock and/or shift register	Limited by detector SNR
Electronic Interface	Complex: N+1 shift registers, 2N D/A converters. All data moves at high speed	Moderate: Only time-dependent values must change
IOC Size	Maximum IOSLM size: N	Maximum IOSLM size: N^2

based upon variations of the engagement algorithm. Once again, this work has its origin in the work of Kung(11) whose systolic alogrithm for matrix-matrix multiplication is shown in Figure 13. Data move through the processor as shown, and each cell performs a running sum of the products of the pairs of values which enter it simultaneously.

A direct integrated optical implementation of Kung's algorithm is shown in Figure 14. It employs electronic shift registers to move the data through a set of herringbone electrooptic multipliers. Addition is performed on summing detectors. An N x N matrix multiplication requires 2N-1 steps, the computation rate being determined by the shift registers. Note that $2N^2$ multiplication elements and $2N^2$ electrical connections are required.

A significant reduction in both the required number of clock steps and the number of components on the IOC is accomplished by using the "compact" engagement architecture shown in Figure 15. This design combines features of both the engagement and parallel IOCs for matrix-vector multiplication. As can be seen, beamsplitters are used to distribute the optical intensities corresponding to the b_{jk} so that they pass under the appropriate a_{ij} modulators. An engagement algorithm is used to assure that data pass through the device in proper synchronism. Since the b_{jk} values are distributed optically, they arrive essentially simultaneously at each of the N a_{ij} modulators at which they are required. It is therefore possible to remove the skew from both matrix element arrays which occurs in the electronic version of the engagement processor.

Comparing Figure 15 to Figure 14 we note that the number of clock steps has been reduced from 2N-1 to N and the number of modulators from $2N^2$ to 2N. Even though the matrix multipliers must each be as wide as N of the vector multipliers the reduction in component count is an advantage since the pin-out number, which will be a limiting factor in a large device, has been greatly reduced. Although we have not attempted to prove the fact, we believe that the compact engagement architecture is the most efficient form for an optical matrix-matrix multiplier.

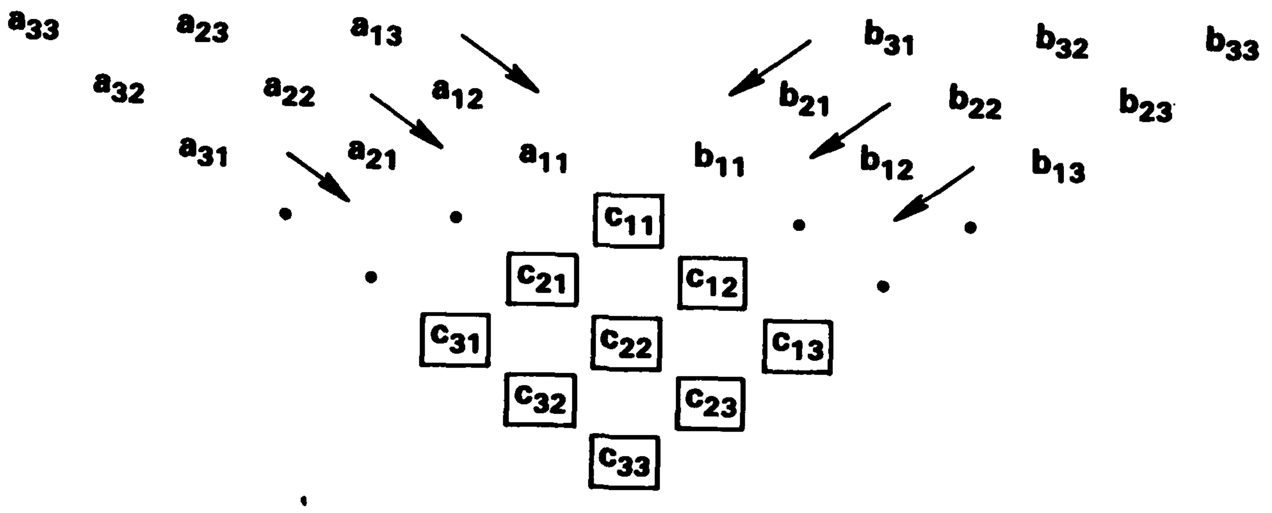

Figure 13. Systolic array architecture for matrix multiplication(11).

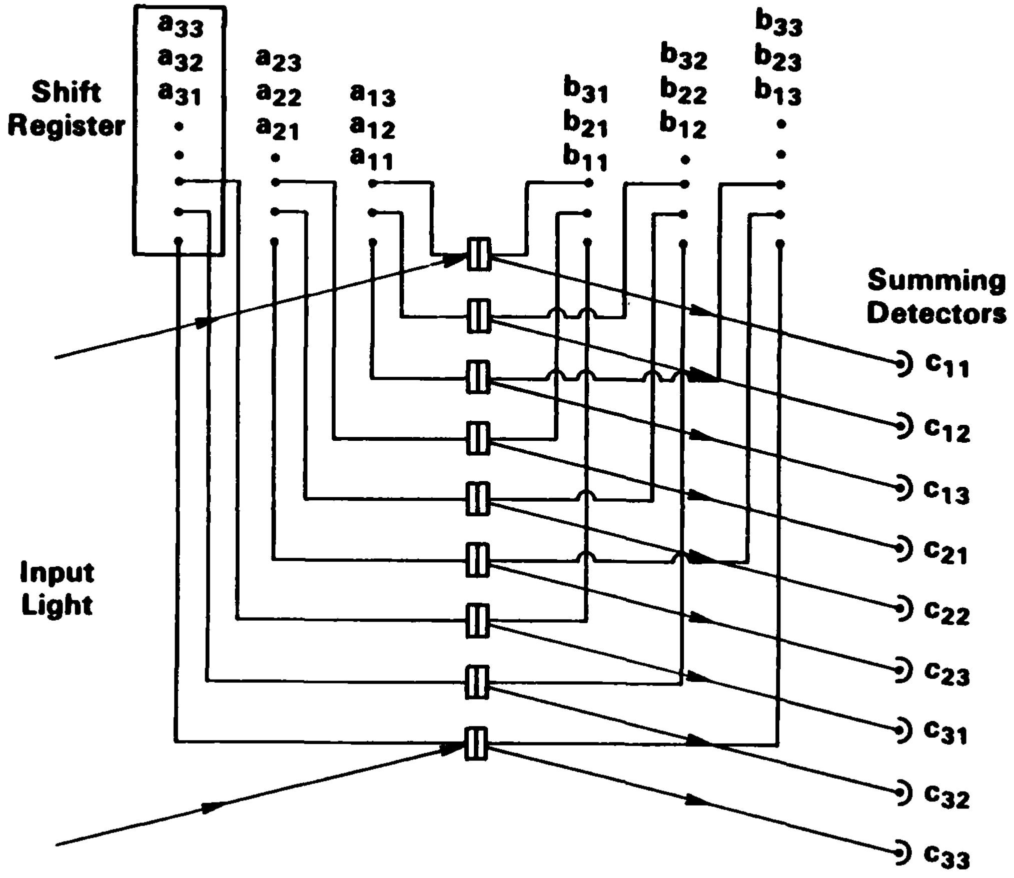

Figure 14. Schematic of an IOC for matrix-matrix multiplication.

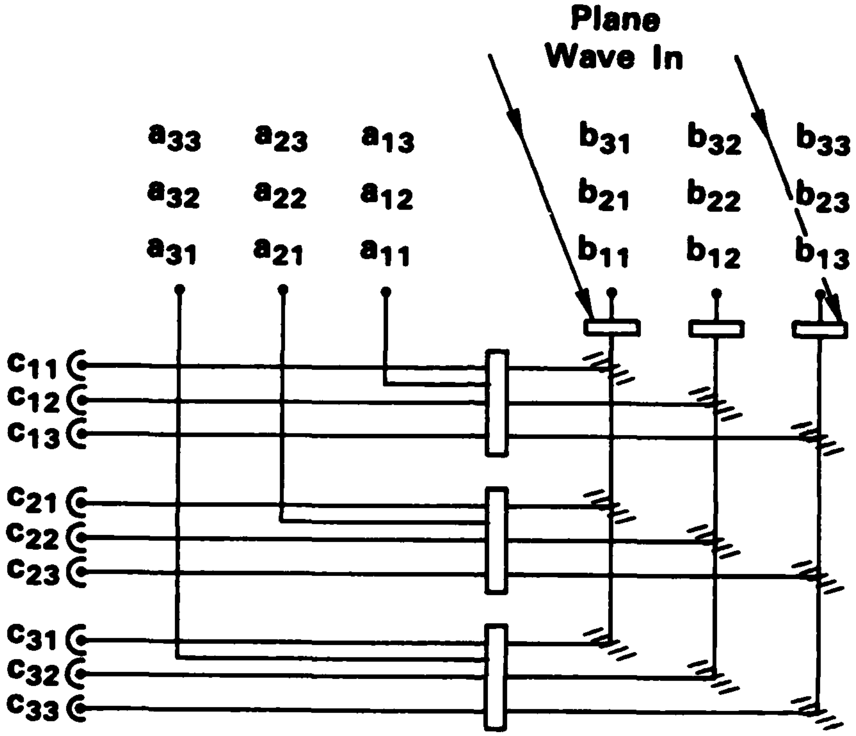

Figure 15. Compact engagement architecture for matrix-matrix multiplication.

IV. AN IOSLM-BASED DIGITAL-TO-ANALOG CONVERTER

During discussions of the device shown in Figure 11, it was pointed out(14) that the large number of A/D converters required by the multiplier could place a large strain on the power budget of the device. This motivated the search for a convenient integrated-optical D/A converter which could be an integral part of the matrix multiplier. The device which was designed(15) in response to this need is shown schematically in Figure 16.

As can be seen in the figure, the integrated-optical D/A converter consists simply of an N-unit IOSLM with each unit biased to have a diffraction efficiency which is a factor of two less than the preceding unit. The total diffracted optical energy is therefore an optical analog of the value of the digital input. The device is therefore an electrical-digital to optical-analog converter. Of course, with the addition of a detector which responds to the total diffracted light, the device can function as a self-contained D/A with electrical input and output.

To demonstrate the operation of the I.O. D/A a six-bit device was assembled and subjected to static tests. The results of one of these tests is shown in Figure 17. The data revealed several small kinks in the output which we believe may have been due to some of the effects which are discussed in Section VI. If this proves to be the case, then it should be easy to design an improved device. Eight-bit accuracy should be attainable at data-rates of hundreds of megawords per second.

Figure 18 shows how the D/A is used as part of an integrated-optical multiplier as originally intended. Note that it is not possible to cascade two of the D/As so the second side of the herringbone must be controlled by an analog signal. The hybrid multiplier can be incorporated into an IOC as suggested in Figure 19. The choice of which input should be digital and which should be analog is, of course, a function of the application.

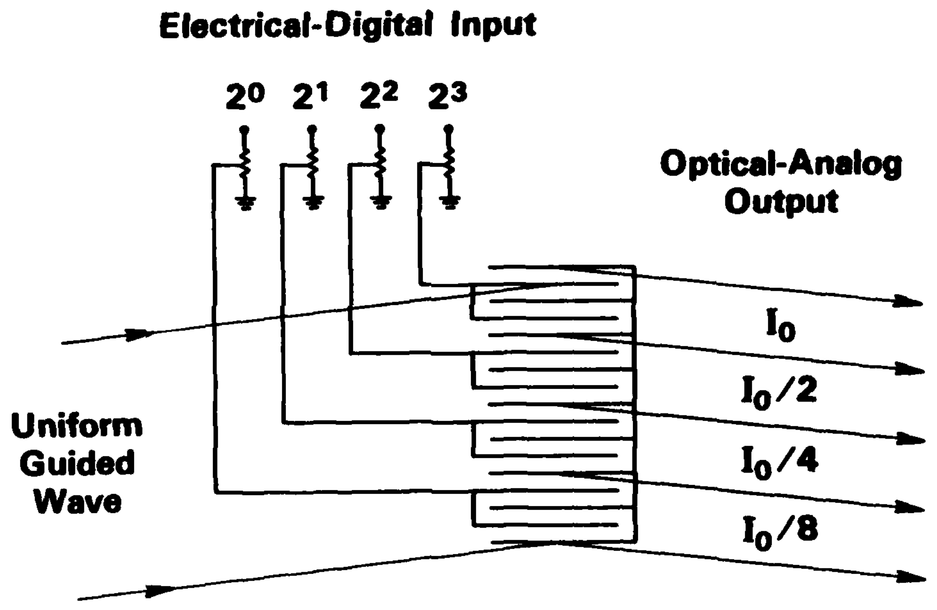

Figure 16. IOSLM-based D/A converter.

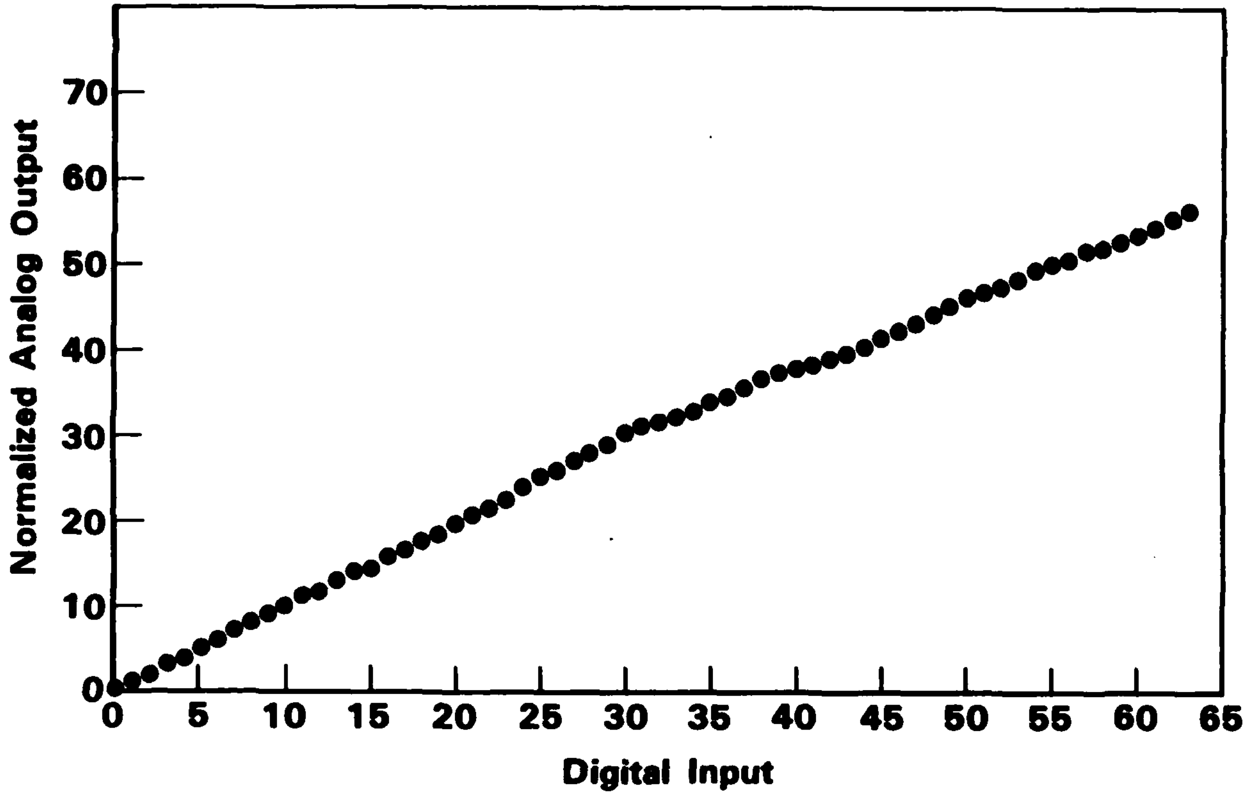

Figure 17. Results of initial dc tests of the IOSLM-based D/A converter.

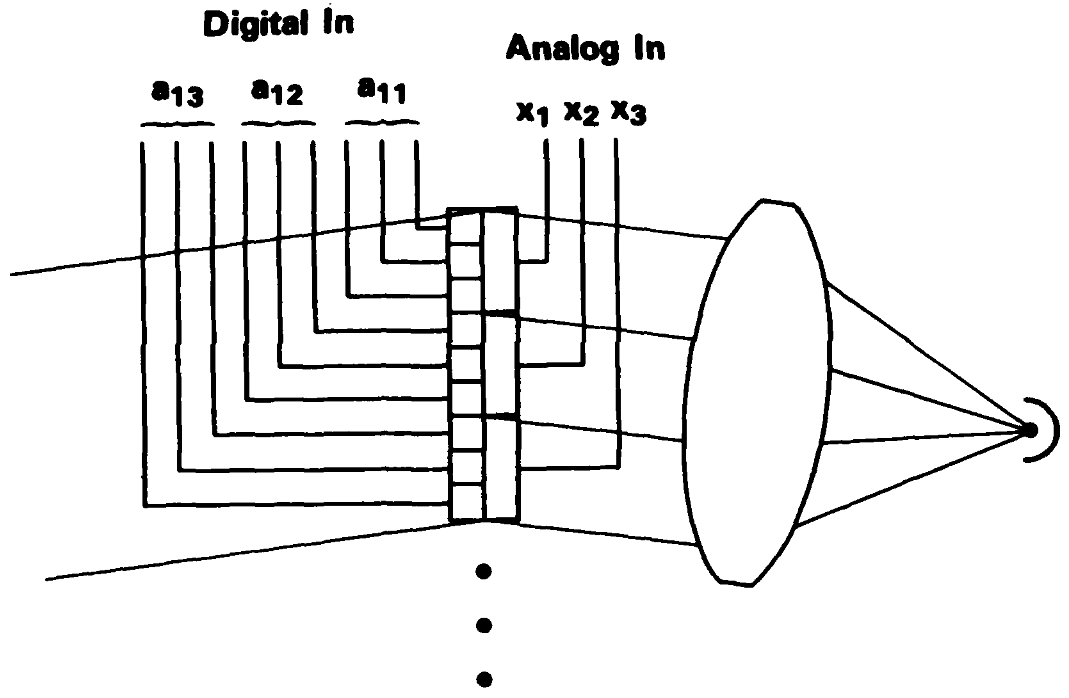

Figure 18. Suggestion for use of IO D/A converter in a hybrid multiplication device.

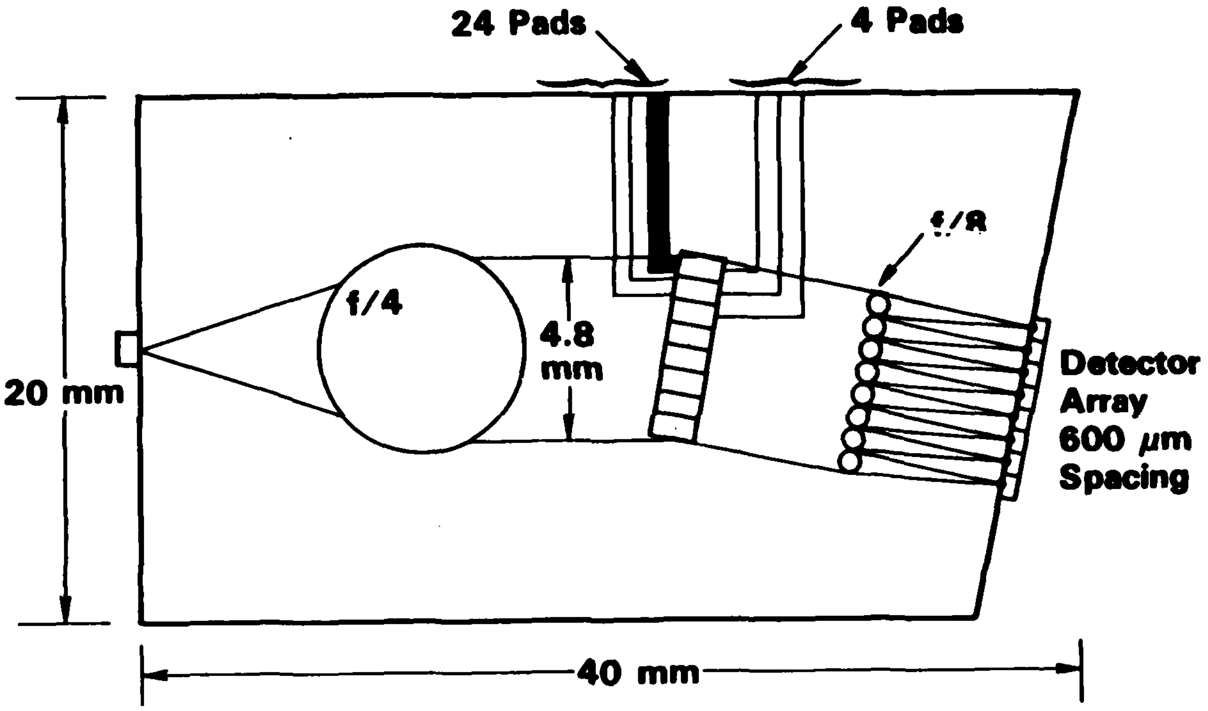

Figure 19. Schematic of an IOC for matrix vector multiplication incorporating electrooptic D/A converters.

V. DESIGN AND FABRICATION OF THE HERRINGBONE ELECTRODE

ELECTRODE DESIGN CONSIDERATIONS

The herringbone electrode structure used for multiplication was discussed briefly in Section II under "Optical Multiplication". It consists of two IOSLM's placed back-to-back so that they share a common spine. The fingers of the gratings are tilted by the Bragg angles so that light entering at Bragg incidence onto one half of the grating array can be diffracted into Bragg incidence onto the other half.

The arrangement using a common spine was chosen in order to keep the spacing between the grating halves in the near field of the diffraction evolution as much as possible. The entire structure is about 4 mm wide so this condition should be fairly well satisfied.

Design of the electrode structure involves several factors that sometimes conflict with one another leading to tradeoffs:

1. It is desired to allow as many segments as possible in order to handle large matrices.
2. It is generally desirable to hold the total beam width to a few millimeters to minimize the variation of the input amplitude across the beam. These variations are due to nonuniformities in the prism coupling spot. When butt-coupled laser diodes are used, these variations will not be present; however, consideration will have to be given to the propagation distance needed to allow beam expansion to a predetermined width. This has an impact on the device length.
3. The individual segments should be kept as high as possible (that is, they should have large apertures) to minimize diffraction spreading and, more important, to minimize the effect of light transmitted through adjacent segments into a given one.
4. The depth of the gratings (length of the finger overlap) should be fairly large to allow high diffraction

efficiency with low drive voltage. This will also tend to reduce second-order diffraction effects.

5. Use of the same period and slant for the two halves simplifies mask fabrication and, very importantly, most nearly matches the output of light diffracted from the first half to the input of the second.
6. Use of different period and slant for the two halves may allow elimination of higher-order diffraction terms.
7. Small periods generate higher fields and larger diffraction angles, improving signal separation; reduce segment size for a given number of finger pairs; reduce second-order diffraction effects; and reduce drive voltage.
8. Small periods tax the photolithographic art, reducing yields; increase the index change, theregy moving away from the Bragg regime towards the Raman-Nath regime; and make the use of a buffer layer more difficult because of the similarity of the buffer thickness to the interelectrode gap.
9. Use of a buffer layer reduces scattering and attenuation, and eliminates the "permanent" grating due to the effective index depression by the metal electrodes.
10. Use of a buffer layer reduces the effective induced index change, thereby increasing drive voltage; and introduces another variable into the fabrication process.

The actual design selected was based upon these factors and previous experience. It was decided first that the device should handle at least 16-dimensional vectors. However, consideration of Factor #3 above led us to choose a 32-segment device. This was done because previous experience with IOSLM shows that the light passing through the sides of the segments can be an appreciable fraction of the light entering the segment. For adjacent channels, this leads to diffracted light that experiences the data from both channels, creating crosstalk and, for a single IOSLM, data-dependent operation. We felt that this situation could only get worse when two gratings were used. At the same time, we wanted to be able to evaluate this effect. With a 32-segment array, we could operate as either 16 data channels separated by one unused guard segment, or as 16 channels without guard segments. In the latter case, we could use channels of double height if desired.

Experience with the IOSLM used in the correlator led us to select a 2 mm grating depth as an acceptable compromise. Mixed experience with buffer layers indicated that the drive voltages might be 3 to 5 times higher than calculated; the 2-mm depth is large enough to keep the drive voltages for 100% diffraction lower than 15 volts when a buffer layer is used.

Since it was anticipated that the herringbone structure would be somewhat more difficult to fabricate than the IOSLM, it was decided to use a 13.6 μm period (3.4 μm linewidths) to relieve demands on the photolithography. This would also allow direct comparison to the earlier IOSLM, which had a similar period. The detailed choice of 13.6 μm was dictated by another factor--the mask is manufactured using a CAD/CAM system at the maskmaker's facility. This facility can produce slant angles accurate to 0.1 degrees. This is not really sufficient to guarantee completely accurate operation of the herringbone, since the Bragg angle is only 0.6 degrees. The period was adjusted to make the Bragg angle an exact multiple of 0.1 degrees, in the hope that this would lead to accurate manufacture. It will be seen later that this hope was not realized.

The final choice was to use identical gratings for the two halves of the electrode. This choice was made for simplicity, since it was believed at that time that the higher-order diffraction terms would not significantly affect operation. This was incorrect, but the exercise allowed us to measure the effect.

The design details of the electrode structure are summarized in Table 2.

Table 2. Design Parameters for First Herringbone Electrode Structure

Item and Units	Value
Grating Depth (mm)	2.0
Grating Period (μm)	13.6
Finger Width (μm)	3.4
Bragg Angle in $LiNbO_3$ (deg)	0.6
Bragg Angle in air (deg)	1.33
Wavelength in Vacuum (μm)	0.6328
Effective Index of $LiNbO_3$ WG	2.21
Number of Segments	32
Number of Finger Pairs/Segment	8
Height of a Segment (μm)	108.8
Required Beam Width (mm)	3.48

DEVICE FABRICATION PROCEDURES

Fabrication of integrated-optical devices is carried out using standardized procedures. The most critical aspects of fabrication are the cleaning of the crystal to accept the Ti film for indiffusion; the indiffusion of the Ti film to form the waveguide; the deposition of a suitable buffer layer to isolate the optical beam from the electrode structure; and the deposition and delineation of the metal film for the electrode structure. The steps for carrying out these fabrication procedures are listed in the tables below.

Table 3. Crystal Cleaning Procedure

1. Blow crystal with nitrogen using electrostatic gun
2. Ultrasonic in DI water/Micro detergent solution
3. Swab clean under running, filtered tap water
4. Rinse in DI water for 2 min
5. Blow dry
6. Polish in Syton colloidal silica for 10 min using 135 g weight
7. Rinse 2 min in DI water and remove from polishing jig
8. Ultrasonic in DI water/Micro/NAOH
9. Swab under filtered tap water and rinse in DI water
10. Immerse in HF 1 min; rinse in DI water; blow dry
11. Rinse in DI water 2 min
12. Immerse in dichromic acid for 3 min
13. Rinse in DI water; blow dry
14. Wipe with Reagent grade methanol and inspect
15. Insert immediately in vacuum system

Table 4. The Ti Deposition Procedure*

1. Pump to 1.2 x 10^{-5} Torr
2. Deposit Ti on substrates at about 18 inches from E-beam gun
3. Remove from system and coat with resist (Shipley AZ 1470J)
4. Monitor thickness with optical flat in place during deposition
5. Bake @85°C for 30 min
6. Cool to room temperature (about 10 min)
7. Expose resist
8. Develop in 5/1, H_2O/Shipley 351 developer (KOH based)
9. Rinse in DI water 1 min+ and blow dry
10. Examine pattern for defects
11. Post-bake @110°C for 20 min
12. Cool to room temperature
13. Etch in solution of 13 pts HF, 6 pts acetic acid, 6 pts nitric acid, 13 pts H_2O
14. Rinse in DI water
15. Examine patterns
16. Strip resist in acetone/methanol solution (50/50)
17. Examine patterns
18. Wipe with methanol
19. Examine for contaminants

*Steps 3 through 18 apply if Ti-pattern delineation is required.

Table 5. The Ti-Indiffusion Procedure

1. Place samples in flat zone of furnace
2. Bring water to desired temperature
3. Begin O_2 flow
4. Bring system to pressure
5. Flow O_2 at approx. 50 cc/min during furnace heat-up
6. Turn on furnace
7. Turn on pre-heater
8. Reduce O_2 flow when furnace reaches temperature to 5-9 cc/min
9. Monitor water temperature, pre-heat temperature, front flow and back flow meters during indiffusion
10. Push boat from flat zone in one push while maintaining pressure and flow
11. Push boat 1 in. per min to 600°C zone
12. Stop flow; maintain pressure
13. Cool overnight
14. Remove and examine under differential-interference-contrast microscope

Deposition of the buffer layer is done using a standard sputtering procedure, using SiO_2 for the layer. The sputtering is usually followed by an annealing step. At the time of manufacture of the layer in the test IOC discussed in the next section, the sputtering method resulted in incompletely oxidized SiO_2. It is believed that this layer then reduces a thin layer at the surface of the waveguide to obtain oxygen. It is known that this tends to increase the conductivity of $LiNbO_3$ and that this increased conductivity will tend to reduce the transfer of the electric field of the electrode pattern to the waveguide. The net result of this is that the voltage required to operate the device is increased, in our case by a factor of about four.

It should be noted that the effects that proceed at the surface of an electrooptic, photorefractive and photoconductive crystal like $LiNbO_3$, in the presence of high fields, light and a reducing overlayer are not presently understood in detail. The simplified discussion given above is based on the assumption of an increased conductivity at the crystal surface due to the incompletely oxidized buffer layer, and a simple analysis of the boundary-value problem for steady-state current flow in conducting layers.

The final step in fabrication consists of the deposition of a thin layer of aluminum over the buffer layer and the delineation, by standard photolithographic techniques, of the electrode pattern. The fabricated device is then mounted into a test jig and leads are attached by wire-bonding to allow characterization of the device. The characterization of one herringbone electrode structure is described in detail in the next section.

VI. STATIC TESTS OF THE HERRINGBONE ELECTRODES

TEST ELECTRONICS

General Driver-Design Considerations

The approach for the driver circuitry was to build a collection of driver stages that could be driven at high switching frequencies, and at a sufficiently high level so as to completely switch the IOC devices.

Because of the large number of devices, space and optical access considerations, it was decided to drive the electrodes via 50-ohm coaxial cable and not attempt to place the active device drivers in close proximity to the IOC device. This dictated that we had to terminate the coaxial cables with 50-ohm loads. Since the switching potentials for the IOC devices were about 7 volts, the design parameters specified called for a 10-volt switching signal. This would result in high power dissipation per device when the driving transistors were switched on. A 10-volt signal across a 50-ohm load requires that we be able to sink a 200mA current. Since we would be driving up to 32 devices, if they were all on at the same time, we would have to supply a current of 6.4 amps.

A significant amount of power was saved by not using a system with a 50-ohm source impedance, but by employing the 50-ohm terminating resistor as the collector load.

One 15 volt high-current power supply is used to drive the IOC loads. One major difficulty with this approach is that as the number of driver transistors that are "on" change, there can be a variation in the bias on these transistors, so that they begin to interact.

The load for each switching transistor consists of the IOC electrode connected between the positive (10V) supply line and the slider of a 100-ohm potentiometer. This potentiometer is in parallel with a 50-ohm, 1W fixed resistor. Thus, the load for the transistor is approximately 50-ohms. The load is situated at the end of a transmission line, so that if any power is reflected back towards the source (the collector of the transistor) it will not be absorbed, but reflected back (in an attenuated form) to the load.

The common electrode of the IOC device is connected to the +10V line supplying the collectors of the output transistors. The potential dividers on each potentiometer thus vary the voltage swing across each electrode with respect to the +10V line.

Driver for Manual Entry of Data

A driver was constructed for static testing of the herringbone device. It consists, in essence, simply of a switch box that allows combinations of segments to be activated in either half or both halves of the electrode array. Up to 32 segments in each half can be addressed. The voltages to be applied are provided in a separate power supply or, if desired, separate power supplies may be used for the two halves of the IOC. This was implemented using a simple switchbox.

Driver for Automatic Data Entry

A controller was designed and constructed, using the principles discussed above under "General Driver-Design Considerations", to allow the automatic application of selected preset voltages to the array segments for dynamic testing of the device. Time and funding did not allow testing of the device using this controller, but the controller is operational and available for use in the next stage of research.

A block diagram of the controller is shown in Fig. 20. Electrode half "A" is addressed from a manually-actuated set of switches to emulate multiplication of a vector by a matrix having constant rows. This was done to avoid the large investment in electronics required for a fully operational multiplier, an investment judged not justified, since the thrust of the research was towards the optical parts of the device.

Electrode half "B" is addressed using a serial word generator, an ECL clock, and shift registers to clock the vector through the herringbone.

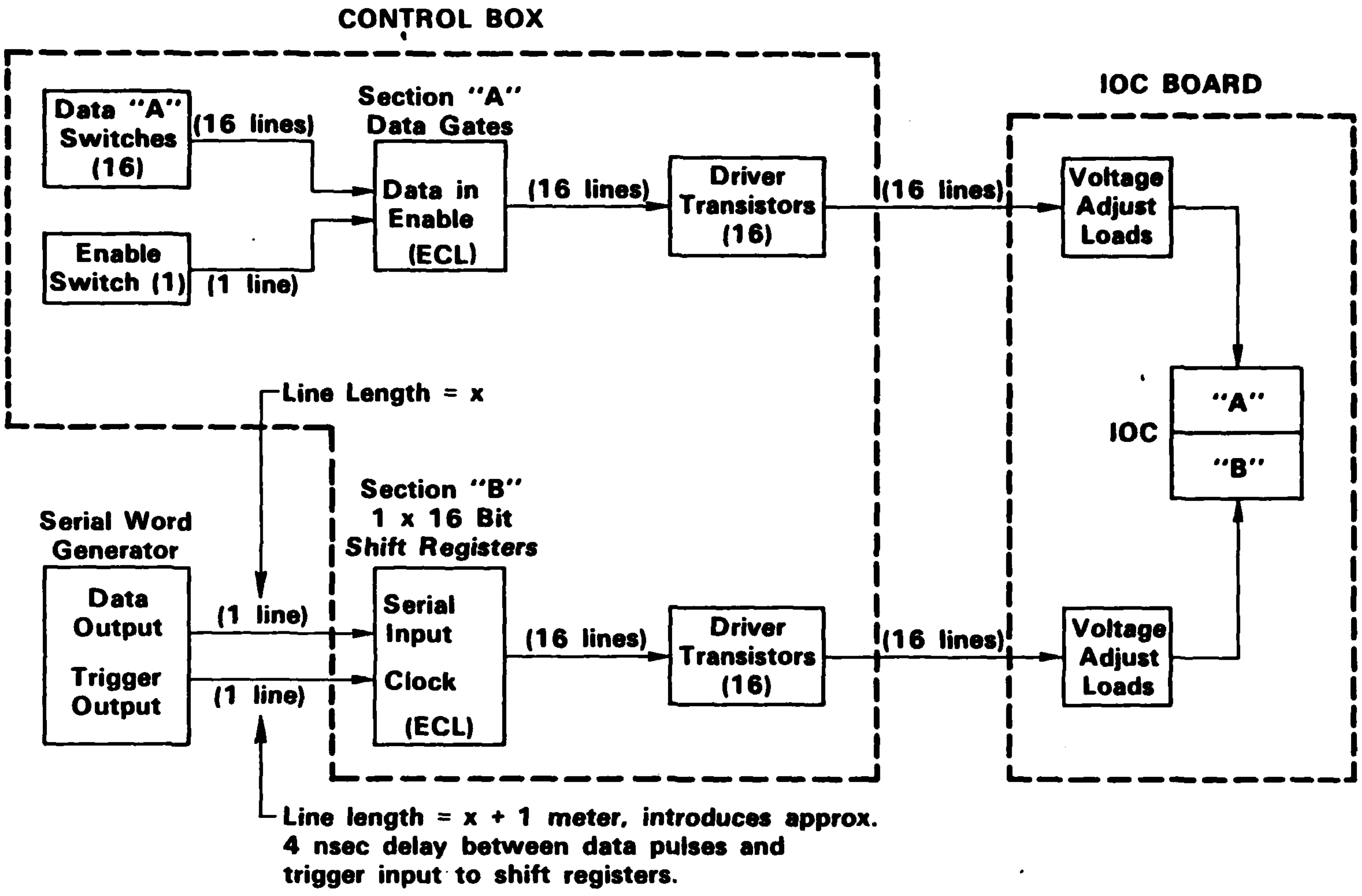

Line length = x + 1 meter, introduces approx. 4 nsec delay between data pulses and trigger input to shift registers.

1 x 16 AUTO MATRIX

Figure 20. Block diagram of controller for automatic data handling.

TEST SETUP

The optical setup for performing the characterization tests consisted basically of a laser, beam-forming optics, and various hardware to allow orientation of the IOC in the test jig for prism coupling of light into and out of the device. Rotation of the device for characterization of the gratings (measurement of Bragg and angles, investigation of second-order diffraction, etc.) was provided by a precision NRC rotator having re-settability, following small angular motions, of about 5 seconds of arc. A drawing of the optical layout is shown in Fig. 21.

TEST RESULTS

Time and funding constraints prevented the carrying out of any dynamic tests. However, one set of herringbone electrodes were characterized fairly completely in static tests. In this section, we will analyze these tests.

A single set of electrodes was fabricated on a Ti:$LiNbO_3$ planar waveguide and leads were bonded for static testing. The sample was flawed, having many unusable segments, but segments 3-16 of both halves were intact. In the static test data to be shown, one half of the electrode array was designated as "A" and the other as "B". Table 6 shows the condition of the arrays.

The first set of tests was run with segments 3-16 of the arrays connected together so that each half of the array operated as a single, long, grating. The direction of maximum diffraction for each angle of Bragg incidence for both grating halves was measured using a precision rotation stage. These data are summarized in Table 7. There are two notable features. First, the Bragg angles, in air, were found to be 1.314 and 1.352 degrees for gratings A and B, respectively. The difference of 0.038 deg is well within the measurement error. The average is 1.333 deg. This is, of course, determined solely by the vacuum wavelength of the light and the grating period. It corresponds to a period of 13.601 μm, and is, within the experimental

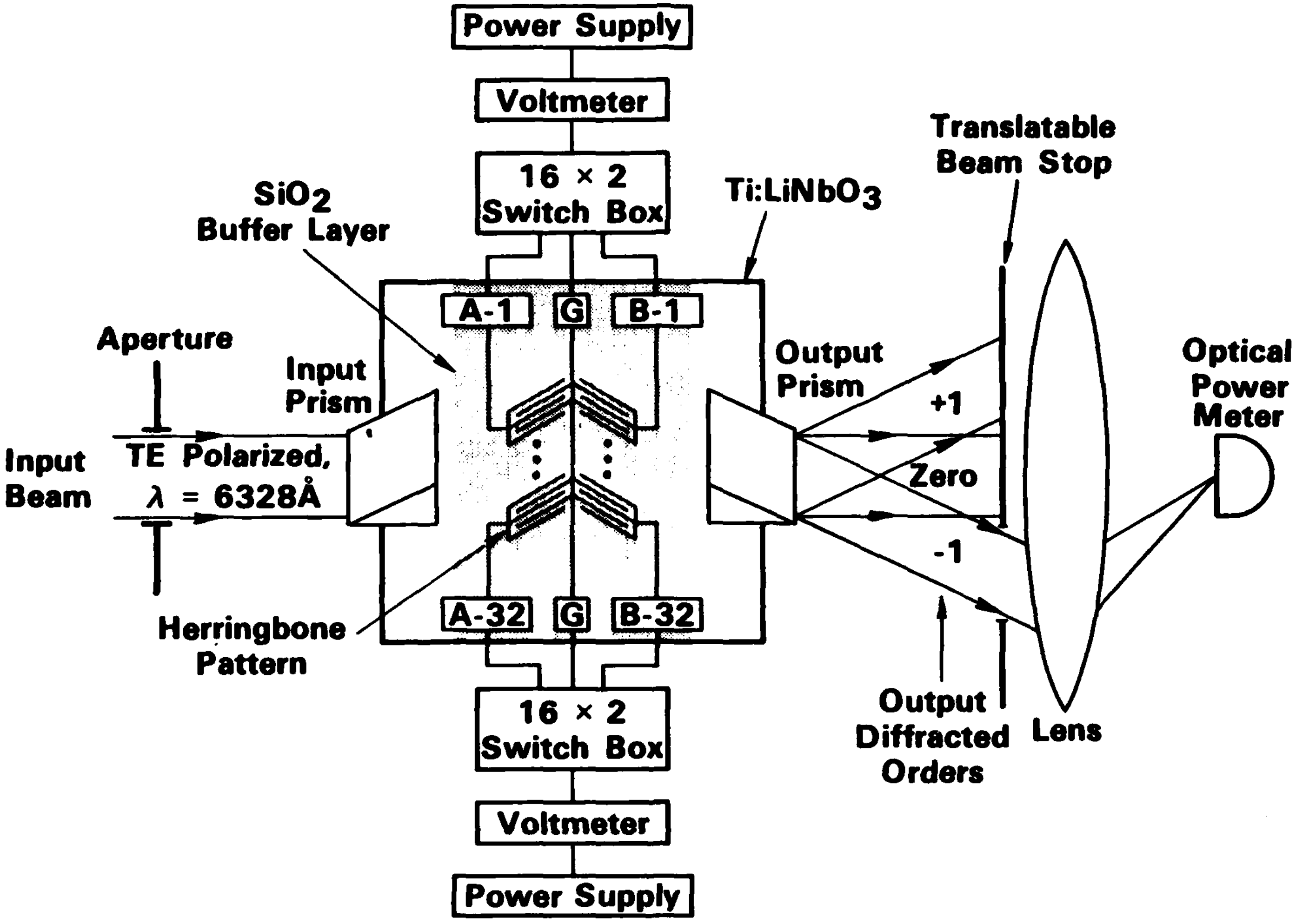

Figure 21. Schematic drawing of experimental setup.

Table 6. Condition of Grating Segments

Segment Number	B(a)	A(a)	Segment Number	B(a)	A(a)
1			17	g	
2		g	18	g	
3	g	g	19	g	g
4	g	g	20	g	g
5	g	g	21	g	g
6	g	g	22	g	g
7	g	g	23	g	g
8	g	g	24	g	g
9	g	g	25		
10	g	g	26		
11	g	g	27		
12	g	g	28		g
13	g	g	29		g
14	g	g	30		g
15	g	g	31		
16	g	g	32		

(a) Note: "g" indicates a good segment, with complete electrical connections.

Table 7. Bragg Data for Electrode Halves

Description	Value (degrees)
(R1) Maximum Diffraction Efficiency for B(at 1° 27' 10")	1.4528
(R2) Turn on A/Extinguish B(at 1° 35' 30")	1.5917
(L1) Maximum Diffraction for B-Other side of O(at 4° 9'25")	4.1569
(R3) Maximum Diffraction for A(at 4° 21' 10")	4.3556
(L2) Maximum Diffraction for A-Other side of O(at 6° 59'0")	6.9833
Calculations:	
Bragg Angle-B in air, degree (L1-R1)/2	1.35205
Bragg Angle-A in air, degree (L2-R3)/2	1.31385
Difference in Bragg Angles (Degrees)	0.0382
Average Bragg Angle, in air (Degrees)	1.3330

error, equal to the design value of 13.600 μm. Second, the measured angle between the fingers of the two grating halves is somewhat larger than the design value of 1.2 deg. The discrepancy is evidenced by the fact that the directions for Bragg incidence above the first grating and below the second grating are not the same, although they were designed to be so. As the data show, these directions differ (in air) by about 0.2 deg., which translates into 0.09 deg on the mask if a 2.21 effective index is assumed. This angle was also measured by observing the far-field diffraction pattern from the gratings when addressed perpendicularly to the waveguide. The average of two such measurements is 1.297 deg., a discrepancy of 0.097 deg. These two measurements give a mask fabrication error averaging 0.094 deg.

Next, the voltage responses of the two gratings were measured. These data are displayed in Fig. 22 and 23. It is seen that the first-order diffracted light follows the expected sinusoidal form quite accurately, with perfect extinction of the incident beam occuring at 14.5 V for grating B, and 99.2% extinction for grating A at the same voltage. It can also be seen that the total power in the sum of the zero- and first-order diffracted beams decreases steadily, indicating that light is either being diffracted into higher orders or that it is being lost some other way, into the substrate for example. Later measurement of light diffracted into the second order revealed 1.5 nW diffracted by grating A with grating B off, and 1.2 nW by grating B with grating A off. While these later measurements cannot be compared directly with the data of the voltage-response curves (since the data were obtained at different times, with the prisms reset between data runs), it does indicate that this second-order diffraction could easily account for the loss of light shown in the figures.

The response of the individual segments, one at a time and in combinations, was measured next. These data were taken at a constant applied voltage of 14.5 V. Table 8 summarizes the data on individual segments for A alone, B alone. It should be noted that the data for A or B alone are very variable. We attribute this to coupling variations across the beam (no effort was made to obtain uniform coupling). This contention is supported by the graph of Fig. 24 and 25. In these figures, the data for the segments of the two gratings (alone) are plotted in the same graph, but the data from grating B is shifted by 1 and 2 positions, respectively. The general

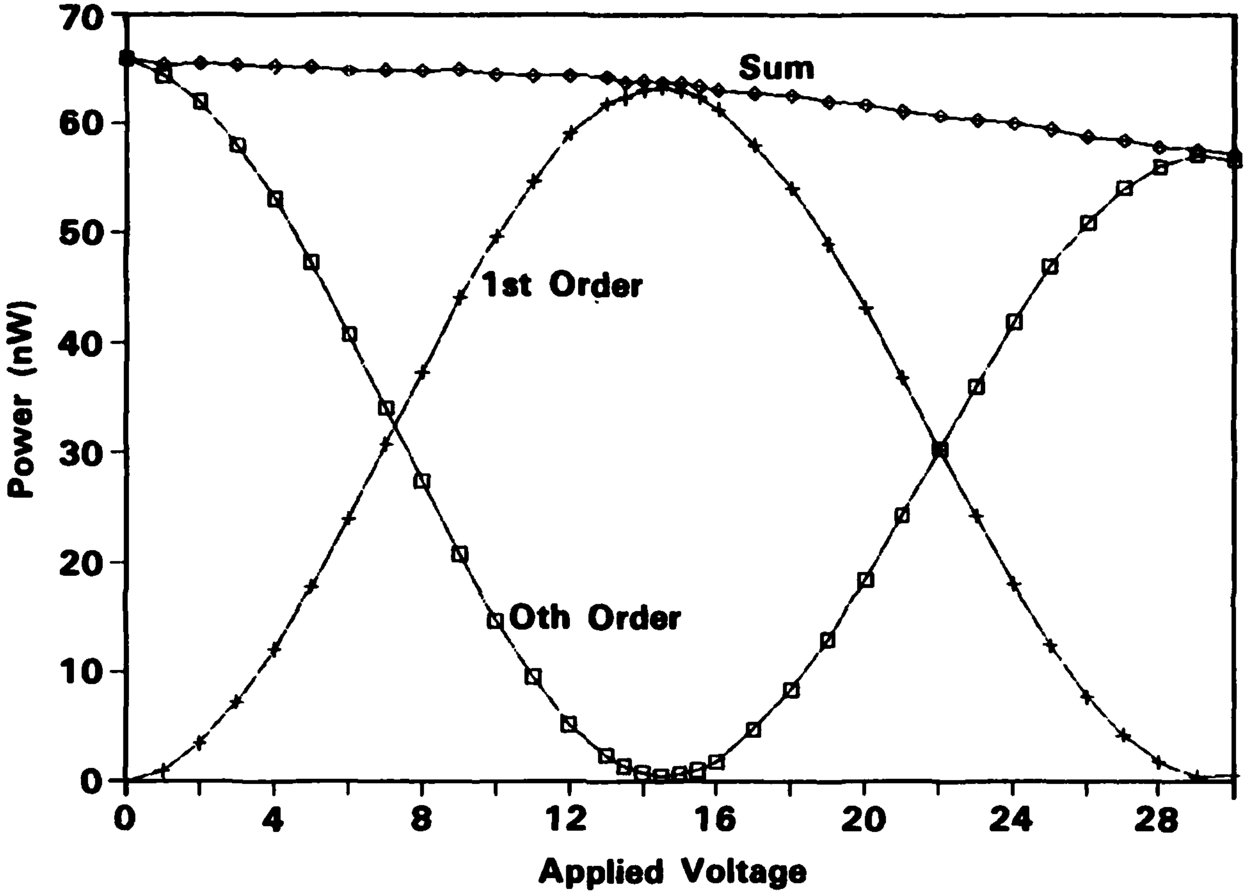

Figure 22. Voltage response for Grating A.

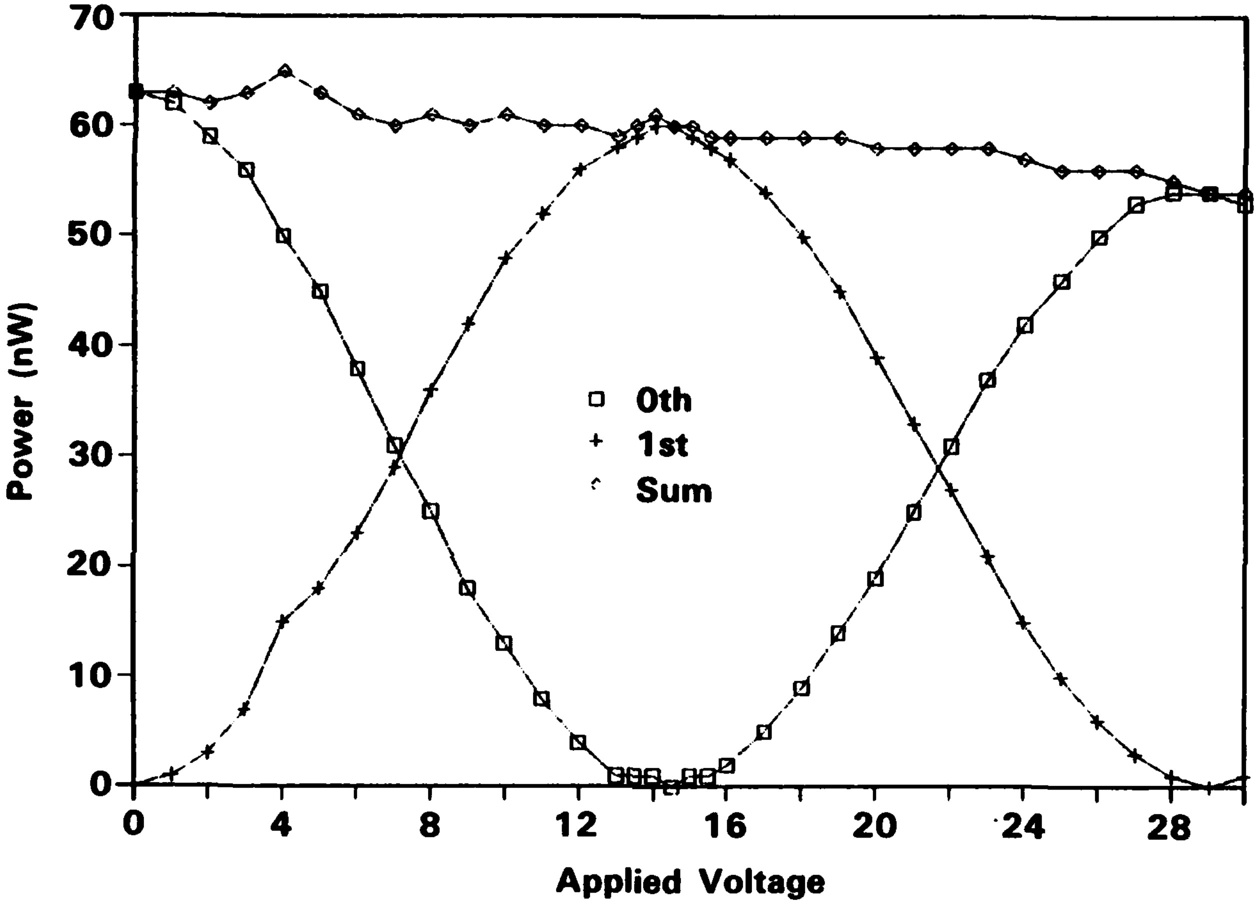

Figure 23. Voltage response for Grating B.

Table 8. Individual Segment and Segment-Combination Data for Each Electrode Half

Segment Number	A,14.5 V Power (nW)	Combinations		Predicted Power (nW)	Segment Number	B,14.5 V Power (nW)	Combinations		Predicted Power (nW)
		Segment On	Power (nW)				Segment On	Power (nW)	
1		3,4	9.3	8.9	1		3,4	9.5	9
2		3,4,5	15.8	14.9	2		3,4,5	13.4	12.5
3	4.7	3,4,5,6	22.7	21.4	3	4.5	3,4,5,6	18.8	17.6
4	4.2	3,4,5,6,7	30.3	28.6	4	4.5	3,4,5,6,7	26.2	24.5
5	6.0	9,10	13.4	13.0	5	3.5	9,10	15.7	15.3
6	6.5	11,12	11.7	11.1	6	5.1	11,12	14.0	13.6
7	7.2	9,10,11,12,13	32.9	30.7	7	6.9	9,10,11,12,13	39.1	34.0
8	7.5	3,5,7,9,11	29.3	29.3	8	7.3	3,5,7,9,11	30.3	30.2
9	6.5	3,7,11,15	22.9	22.9	9	8.4	3,7,11,15	26.4	26.4
10	6.5	3-16	92	84.4	10	6.9	3-16	100.6	89.4
11	4.9				11	6.9			
12	6.2				12	6.7			
13	6.6				13	5.1			
14	6.1				14	7.6			
15	6.1				15	8.1			
16	5.4				16	7.9			

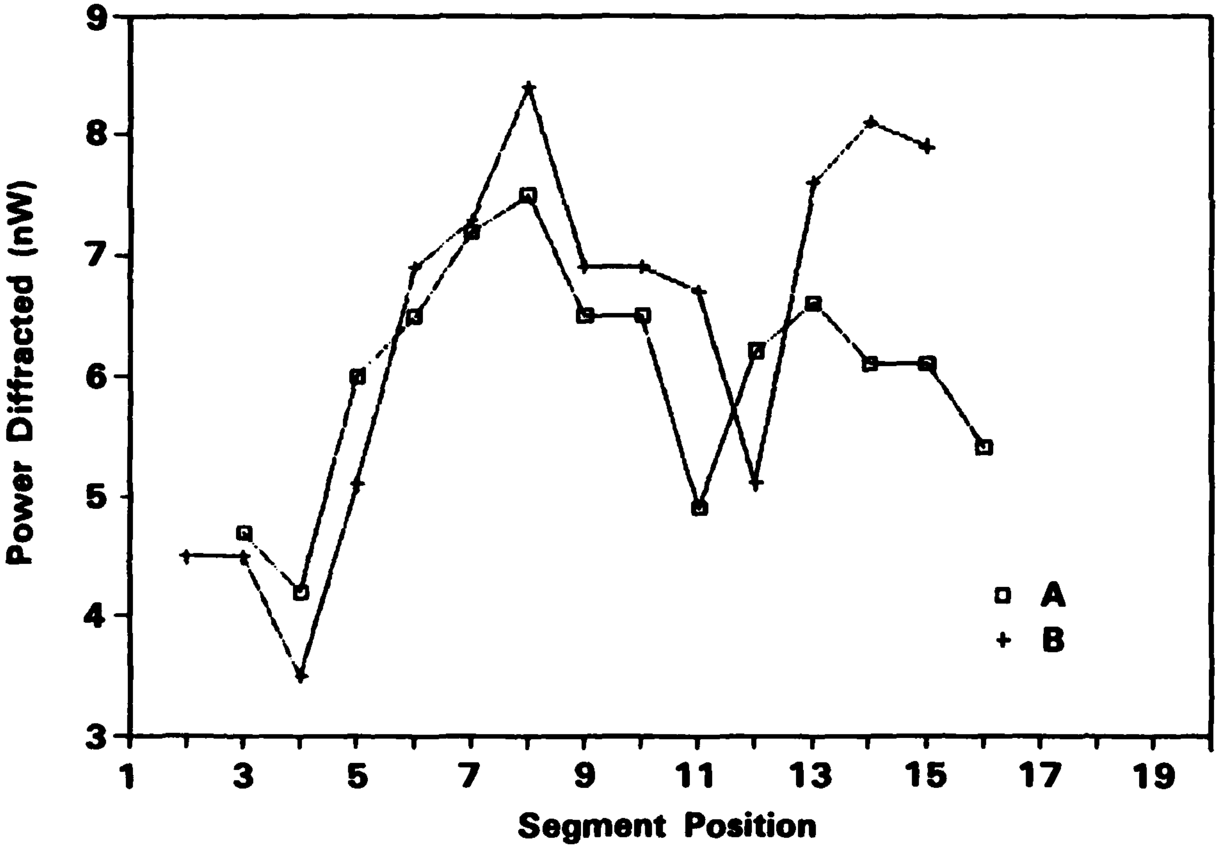

Figure 24. Diffractive power vs segment position. Data for Grating B has been shifted by one position.

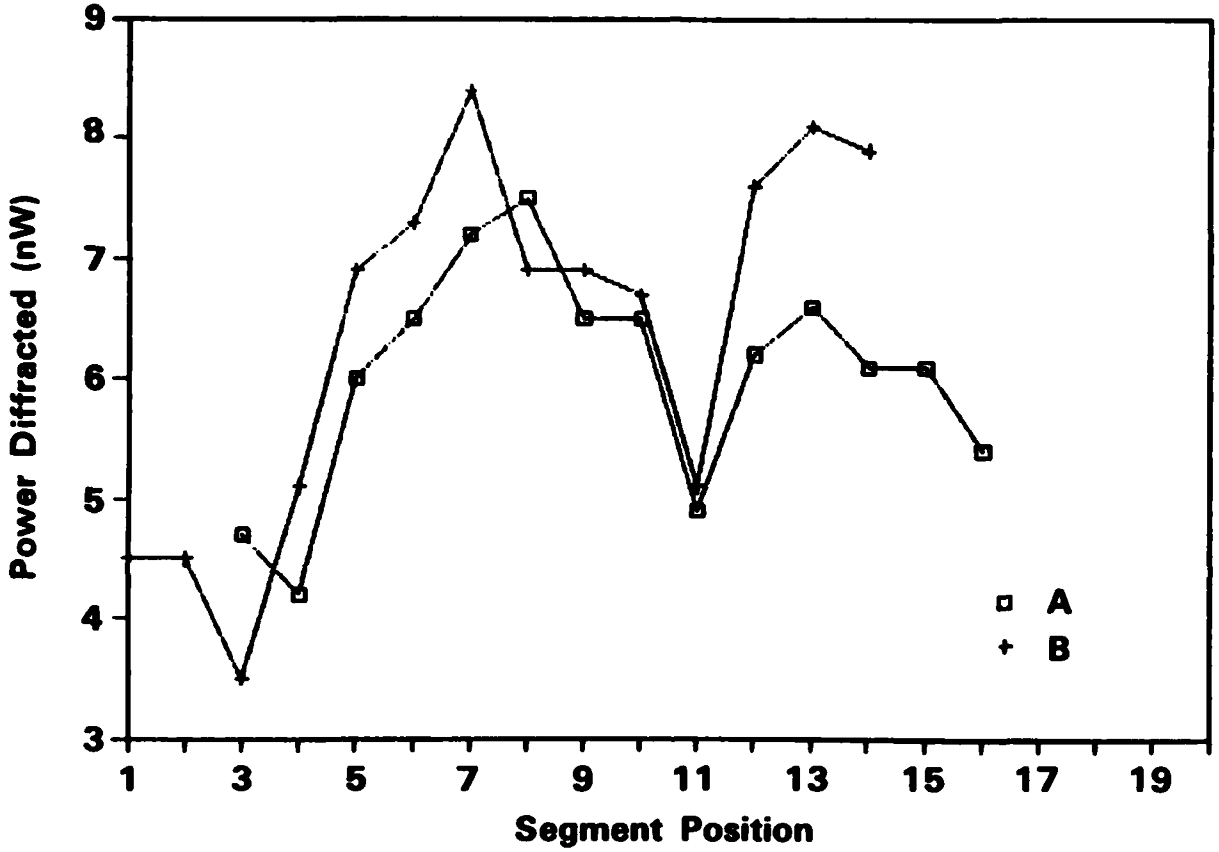

Figure 25. Diffractive power vs segment position. Data for Grating B has been shifted by two positions.

similarity of the curves is striking, especially the sharp coincidence of the minima. The drift away from coincidence at one minimum when the other is forced can be explained by the rotation needed to go from Bragg incidence on A to Bragg incidence on B.

Also shown in Table 8 are data taken with various combinations of segments turned on. These data were taken to investigate the effect of adjacent segments on one another. It is easily seen that the diffracted power from several adjacent segments is always higher than is predicted from the sum of the individual segment data. The data for the cases where alternate segments are activated, however, follows accurately the predictions based upon the sum of the individual segment outputs, indicating that a single guard (unactivated) segment is adequate protection. Data is also shown for activation of every fourth segment; it, too, is predictable from individual segment data.

Finally, measurements were taken, similar to that for the individual gratings, for situations where both halves of a segment are activated, accomplishing the multiplication operation. These data are displayed in Table 9. The coupling prisms were reset for each data set. Two sets of product data are shown. The individual segment pairs show the same variation from the coupling spot as was shown by the individual segments for each grating half. Also, the data for activation of alternate segments again follows the results predicted from the individual segment data accurately, while the data for adjacent segments shows the same edge effects as did the data for the grating halves.

The columns labeled "Other Combinations" display a variety of combinations of segments from A and B, either alone or in combination with one another. The numbers are the activated segments of each grating. We can see the effect of second-order diffraction, even with only a single segment (#8) activated in A or B alone. A activated alone contributes 2.0 nW to the product output direction; A and B activated together contribute 58.0 nW. Hence, the second-order diffraction from segment 8 is 3.4% of the product data. For gratings 3-16 activated, the result is about 1.4%.

Table 9. Product Data for Individual Segments and for Segment Combinations

	Data Set 1							Data Set 2						
	A+B	Multiple Segments 14.5 V			Other Combinations			A+B	Multiple Segments 14.5 V			Other Combinations		
Segment Number	(14.5V) (nW)	Segment Numbers	Power (nW)	Sum (nW)	On A	On B	Power (nW)	(14.5V) (nW)	Segment Numbers	Power (nW)	Sum (nW)	On A	On B	Power (nW)
1		3,4	9.8	8.2	0	0	0.00		3,4	9.8	8.8	3-16	0	1.5
2		3,4,5	12.9	11.3	8	8	5.80		3,4,5	14.6	12.4	0	3-16	1.2
3	3.9	3,4,5,6	18.2	15.9	8	0	0.20	3.9	3,4,5,6	21.4	18.1	0	0	0
4	4.3	3,4,5,6,7	25.8	21.8	-	8	0.10	4.9	3,4,5,6,7	29.9	24.8			
5	3.1	9,10	13.2	11.2	8	7	0.30	3.6	9,10	15.0	12.5			
6	4.6	11,12	10.6	9.6	8	7,9	0.50	5.7	11,12	12.9	10.7			
7	5.9	9,10,11,12,13	28.4	24.1	7	8	0.30	6.7	9,10,11,12,13	35.3	27.6			
8	5.8	3,5,7,9,11	23.8	24.1	7,9	8	0.50	6.9	3,5,7,9.11	26.9	27.0			
9	5.9	3,7,11,15	18.8	19.1	3,5...,15	2,4,...,16	1.60	6.8	3,7,11,15	23.0	23.0			
10	5.3	3-16	77.3	64.9	0	0	0.00	5.7	3-16	101.2	78.9			
11	5.3							6.0						
12	4.3							4.7						
13	3.3							4.4						
14	4.6							6.4						
15	4.0							6.4						
16	4.6							6.8						

The assertion that these effects are due to second order diffraction is confirmed by the data presented in Figure 26. Here we display the intensities of the 2nd-order and -1st order diffracted beams (whose sum comprises the second-order diffraction) as a function of applied voltage, along with the 0th- and 1st-orders. These results, which are in good qualitative agreement with the theory of Mohoram and Young,(16) explain the discrepancies between measurement and expectation as displayed in Table 9, and account for essentially all of the light emerging from the electrooptic grating.

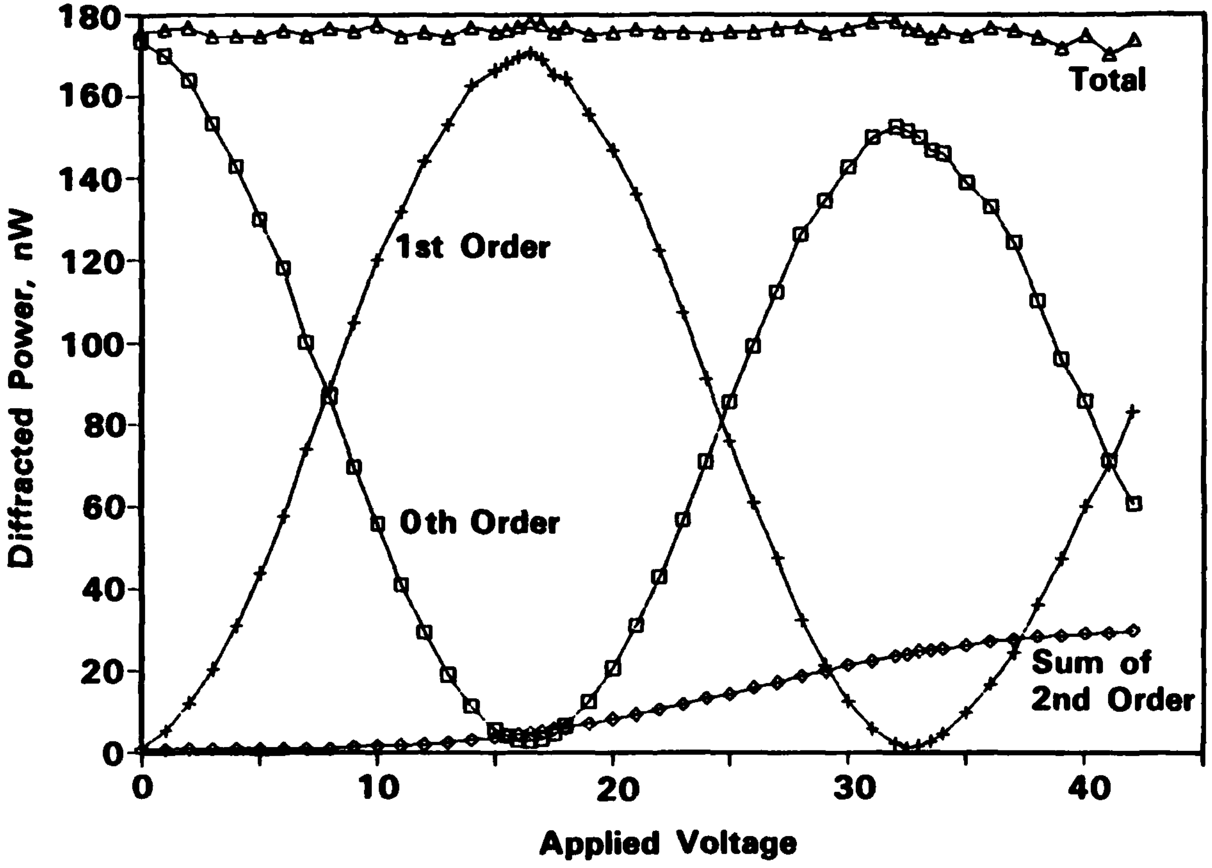

Figure 26. Multiple diffracted orders from an electrooptic grating. As can be seen at higher voltages there is a significant higher order contribution.

CONCLUSIONS

The integrated-optical device designs which were developed for the implementation of several matrix-multiplication algorithms clearly indicate there are several ways in which I.O. technology can contribute to the general area of optical computation. The compact architecture developed here would, in fact, seem to be the highest-spped approach to matrix-matrix multiplication yet suggested.

The preliminary experimental results indicate the potential for system linearity of at least ± 0.5% which is the accuracy to which data were taken. This corresponds to 7 bit accuracy in a binary system.

The data also indicate two avoidable potential sources of error in the herringbone device. The first of these is crosstalk which can be entirely eliminated by the introduction of guard bands between the active device segments. The tradeoff here is that about one-third of the light coupled into the IOC is not used in the generation of data.

The second source of error is due to second-order diffraction effects. There was seen to be about a 3% effect which can be reduced and perhaps entirely eliminated in two ways. The first, and surest approach is the use of an asymmetric herringbone structure so the 2^{nd}-order output of the first grating does not emerge in the same direction as the doubly-diffracted light. The second approach is to use a higher grating frequency and/or longer grating fingers, both of which will supress the 2^{nd}-order effects.

We therefore conclude that, using the IOC architectures developed during the course of this program, and using the existing data to design a second generation of multiplication elements, it will be possible to build a family of high-speed integrated-optical devices for matrix-vector and matrix-matrix multiplication.

REFERENCES

1. R. V. Schmidt and I. P. Kaminow, "Metal Diffused Optical Waveguides in $LiNbO_3$", Appl. Phys. Lett. 25, 458 (1974).

2. G. L. Tangonan, D. L. Persechini, J. F. Lotspeich and M. K. Barnoski, "Electrooptic Diffraction Modulation in Ti-Diffused $LiTaO_3$", Appl. Opt. 17, 3259 (1978).

3. H. Kogelnik, "Coupled Wave Theory for Thick Hologram Gratings", Bell Syst. Tech. J., 48, 2909 (1969).

4. I. P. Kaminow, Introduction to Electrooptic Devices, (Academic Press, New York, 1974).

5. I. P. Kaminow and L. W. Stulz, "A Planar Electrooptic-Prism Switch", IEEE J. of Quant. Electr. QE-11, 633 (1975).

6. J. M. Hammer and W. Phillips, "Low-Loss Single-Mode Optical Waveguides and Efficient High-Speed Modulators of $LiNb_xTa_{1-x}O_3$ on $LiTaO_3$", Appl. Phys. Lett. 24, 545 (1974).

7. R. L. Holman and P. J. Cressman, "A Very High Throughput Damage-Resistant Lithium Niobate Waveguide Modulator", Topical Meeting on Integrated and Guided-Wave Optics, Incline Village, NV, January 28-30, 1980, Technical Digest, Paper TuE6.

8. C. M. Verber, R. P. Kenan and J. R. Busch, "Correlator Based on an Integrated Optical Spatial Light Modulator", Appl. Opt. 20, 1626 (1981).

9. J. W. Goodman, A. R. Dias and L. M. Woody, "Fully-Parallel, High-Speed Incoherent Optical Method for Performing Discrete Optical Transforms", Opt. Lett. 2, 1 (1978).

0. C. M. Verber and R. P. Kenan, "Integrated Optical Circuits for Numerical Computation", Proc. SPIE 408, 57-64 (1983).

11. H. T. Kung, "Why Systolic Architectures?" Computer 15, 37 (1981).

12. H. J. Caulfield, W. J. Rhodes, M. J. Foster and Sam Horvitz, "Optical Implementation of Systolic Array Processing", Opt. Comm. 40, 86 (1981).

13. P. Tamura, private communication.

14. M. Hamilton, private communication.

15. C. M. Verber and B. T. Smith, "An Integrated Optical D/A Converter", Appl. Opt. 22, 3677 (1983).

16. M. G. Moharam and L. Young, "Criterion for Bragg and Raman-Nath Diffraction Regimes, Appl. Opt. 17, 1757 (1978).